Geochemistry Geophysics Geosystems G3

Article
Volume 13, Number 10
30 October 2012
Q10022, doi:10.1029/2012GC004286
ISSN: 1525-2027

Published by AGU and the Geochemical Society

Copper-nickel-rich, amalgamated ferromanganese crust-nodule deposits from Shatsky Rise, NW Pacific

J. R. Hein and T. A. Conrad
U.S. Geological Survey, 400 Natural Bridges Drive, Santa Cruz, California 95060, USA (jhein@usgs.gov)

M. Frank
GEOMAR, Helmholtz Centre for Ocean Research Kiel, Wischhofstrasse 1-3, DE-24148 Kiel, Germany

M. Christl
Laboratory of Ion Beam Physics, ETH Zurich, Schafmattstrasse Co, CH-8093 Zurich, Switzerland

W. W. Sager
Department of Oceanography, Texas A&M University, College Station, Texas 77843, USA

[1] A unique set of ferromanganese crusts and nodules collected from Shatsky Rise (SR), NW Pacific, were analyzed for mineralogical and chemical compositions, and dated using Be isotopes and cobalt chronometry. The composition of these midlatitude, deep-water deposits is markedly different from northwest-equatorial Pacific (PCZ) crusts, where most studies have been conducted. Crusts and nodules on SR formed in close proximity and some nodule deposits were cemented and overgrown by crusts, forming amalgamated deposits. The deep-water SR crusts are high in Cu, Li, and Th and low in Co, Te, and Tl concentrations compared to PCZ crusts. Thorium concentrations (ppm) are especially striking with a high of 152 (mean 56), compared to PCZ crusts (mean 11). The deep-water SR crusts show a diagenetic chemical signal, but not a diagenetic mineralogy, which together constrain the redox conditions to early oxic diagenesis. Diagenetic input to crusts is rare, but unequivocal in these deep-water crusts. Copper, Ni, and Li are strongly enriched in SR deep-water deposits, but only in layers older than about 3.4 Ma. Diagenetic reactions in the sediment and dissolution of biogenic calcite in the water column are the likely sources of these metals. The highest concentrations of Li are in crust layers that formed near the calcite compensation depth. The onset of Ni, Cu, and Li enrichment in the middle Miocene and cessation at about 3.4 Ma were accompanied by changes in the deep-water environment, especially composition and flow rates of water masses, and location of the carbonate compensation depth.

Components: 16,700 words, 8 figures, 9 tables.

Keywords: age dating; deep-water; diagenetic crusts; ferromanganese crusts and nodules; high Cu, Ni, Li, Th; mid-latitudes.

Index Terms: 0461 Biogeosciences: Metals; 1050 Geochemistry: Marine geochemistry (4835, 4845, 4850); 1065 Geochemistry: Major and trace element geochemistry.

Received 12 June 2012; **Revised** 10 September 2012; **Accepted** 26 September 2012; **Published** 30 October 2012.

Hein, J. R., T. A. Conrad, M. Frank, M. Christl, and W. W. Sager (2012), Copper-nickel-rich, amalgamated ferromanganese crust-nodule deposits from Shatsky Rise, NW Pacific, *Geochem. Geophys. Geosyst.*, *13*, Q10022, doi:10.1029/2012GC004286.

1. Introduction

[2] Most previous regional studies of ferromanganese oxide crusts (Fe-Mn crusts) utilized samples collected from relatively shallow water (above 3000 m water depth) on seamounts and ridges located in the northwest-equatorial Pacific region, within about 20° latitude of the equator in a corridor from Hawaii to the west Pacific trenches. That geographic focus was due to the occurrence of old and large seamounts/guyots in that region and the high concentrations of cobalt, the metal presently of greatest economic interest in those shallow-water crusts [*Hein et al.*, 2009]. That region is the Prime Crust Zone (PCZ) of greatest economic interest in the global ocean [*Hein et al.*, 2009] and is therefore one of the areas used for comparisons with the Shatsky Rise crusts.

[3] We report here on the occurrence, composition, age, and origin of a unique set of Fe-Mn crust, nodule, and amalgamated crust-nodule deposits sampled from relatively deep water (mostly below 3000 m depth) at middle northern latitudes (32°–40°) on Shatsky Rise (Figure 1). These Fe-Mn deposits from Shatsky Rise have chemical compositions markedly different from those in the PCZ and from the open-ocean Pacific and global crusts in general.

2. Background

[4] There have been four primary areas of focus in the study of Fe-Mn crusts, their distribution, composition, and mechanisms of formation; their economic potential for Co, Mn, rare earth elements (REEs), Ti, Ni, Mo, Pt, Zr, Te, Cu, W, and others; the use of Fe-Mn crusts as recorders of the past 70 million years (Ma) of oceanic and climatic history; and the role that the global complement of crusts (and nodules) play in the geochemical balance of the oceans. This work predominantly focuses on the first of those four.

[5] Fe-Mn crusts occur on hard-rock substrates and nodules on sediment-covered abyssal plains and plateaus throughout the global ocean. Crusts form at the seafloor on the flanks and summits of seamounts and ridges where the rocks have been swept clean of sediments for millions of years [*Hein et al.*, 2000]. Crusts can be up to 260-mm thick and form pavements on rock outcrops by way of hydrogenetic precipitation from cold ambient bottom waters. Crusts form at water depths between ~400–7000 m, with the thickest and most metal-rich crusts occurring at depths of ~800–2500 m. The mean dry bulk density of crusts is 1.3 g/cm^3, the mean porosity is 60%, and they are characterized by an extremely high mean surface area averaging 325 m^2/g [*Hein et al.*, 2000]. Crusts generally grow at remarkably slow rates of 1–5 mm/Ma [e.g., *Hein et al.*, 2000]. The extensive surface area and slow growth rates allow for the adsorption of many elements from seawater in high concentrations.

[6] In general, the dominant controls for the concentration of metals in Fe-Mn crusts are the concentration of metals in seawater and their ratios, colloid surface charge, types of complexing agents, stability of surface complexes, surface oxidation reactions, specific-surface area, and growth rates. More specifically, a first-order electrochemical model proposes that positively charged species dissolved in seawater will adsorb onto the negatively charged MnO_2 surfaces and neutral and negatively charged species will adsorb onto the slightly positively charged surfaces of FeO(OH) [*Koschinsky and Halbach*, 1995; *Koschinsky and Hein*, 2003] at the pH of seawater (~8). Some sorbed metals are oxidized to more stable states at the colloid surface thereby facilitating higher concentrations than would otherwise be possible [e.g., *Murray and Dillard*, 1979; *Bidoglio et al.*, 1993].

3. Geomorphology and Geological Setting

[7] Shatsky Rise is about 450 km wide and 1650 km long and resides on Late Jurassic and Early Cretaceous lithosphere that becomes younger to the northeast [*Nakanishi et al.*, 1999; *Sager et al.*, 1999]. Substantial outpourings of basalt occurred at least three times forming three plateaus separated by deep-water areas that are only a few hundred meters above the regional baseline (Figure 1). These three plateaus were informally named TAMU, ORI, and Shirshov by *Sager et al.* [1999]. TAMU plateau is by far the largest in area and volume and was the first to form. A ^{39}Ar-^{40}Ar radiometric age of 144.6 ± 0.8 Ma was determined from massive flows cored at IODP Site 1213 on the south flank of TAMU [*Mahoney et al.*, 2005]. Two other volcanic features occur in close proximity to Shatsky Rise. Papanin Ridge forms an apparent northeast extension of the Rise but is separated from it by a deep trough; and the Ojin Rise Seamounts, which partly sit on a swell and form a chain trending east-northeast away from Shirshov plateau (Figure 1). Both these volcanic structures may be connected with Hess Rise to the east.

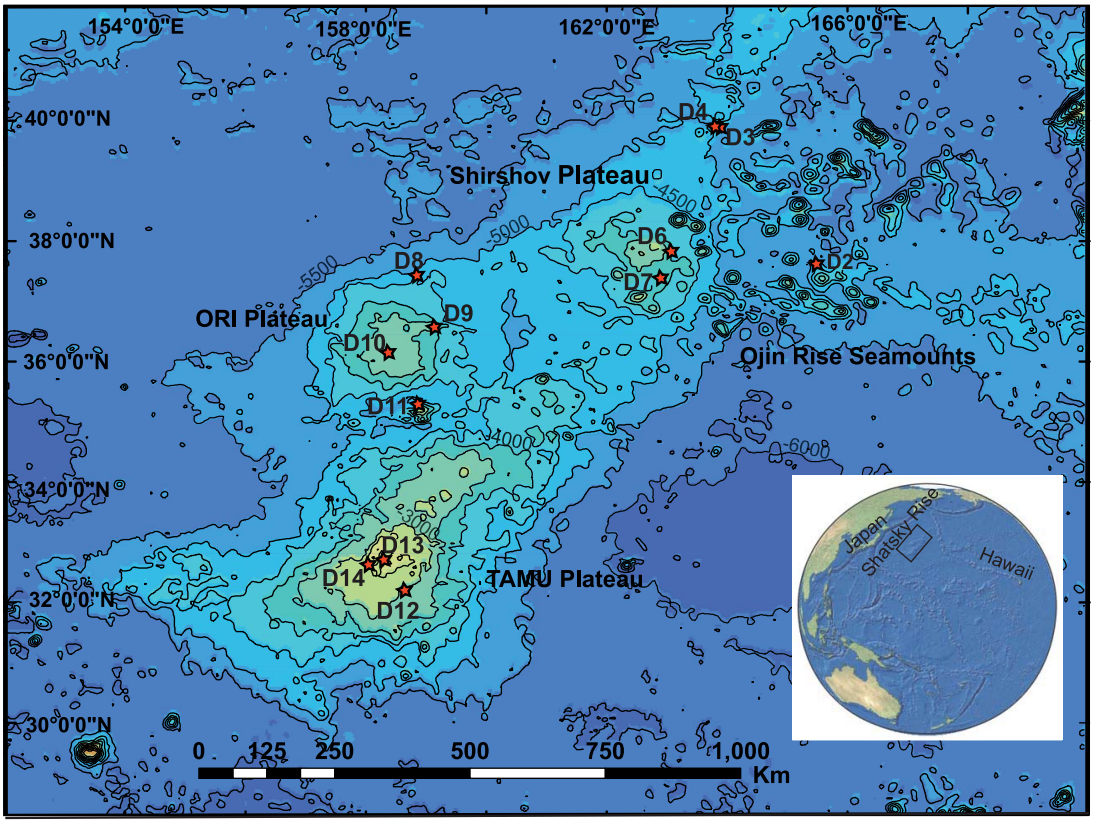

Figure 1. Location of Shatsky Rise (inset), the three plateaus that make up the Rise, and dredge sites D2–D14 from which Fe-Mn deposits were collected.

[8] The regional seafloor ranges in depth from about 5500 to 6000 m and the entire approximately 480,000 km^2 area of Shatsky Rise can be outlined by the 5000 m isobath, with depths as shallow as about 2000 m, but typically are greater than 3000 m [*Sager et al.*, 1999]. Shatsky Rise is covered at its summits by up to 1.2 km of mostly Cretaceous pelagic carbonates, in contrast to less than 500 m of sediment on the surrounding abyssal plain. Sediments on the flanks of Shatsky Rise are thin with comparable thickness to surrounding abyssal sediments [*Sager et al.*, 1999]. Ridges and seamounts on Shatsky Rise are clear of sediment in many places and these sediment-free areas are the locations of Fe-Mn crust formation.

[9] Shatsky Rise formed rapidly [*Sager and Han*, 1993] although episodically during three stages that formed the three plateaus [*Mahoney et al.*, 2005]. Formation occurred predominantly near an oceanic ridge-ridge-ridge triple junction [*Nakanishi et al.*, 1999]. It was proposed that the Rise formed from a mantle plume head and decompressional melting [*Sager et al.*, 1999], with Papanin Ridge having formed from the mantle plume tail. However, subsequent work showed that the few rocks that have been analyzed from Shatsky Rise have MORB-like and not OIB-like geochemical and petrographic characteristics [*Tatsumi et al.*, 1998; *Mahoney et al.*, 2005]. These new data are consistent with either a perisphere or meteorite-impact origin [*Mahoney et al.*, 2005; *Sager*, 2005]. Ojin Rise Seamounts may have formed somewhat later from a different magmatic source.

[10] Although the principal plateaus of Shatsky Rise currently lie at latitudes from 30 to 40°N, paleomagnetic data indicate that the plateau was near the equator during its formation and subsequently drifted northward by ~35° [*Sager*, 2006]. Northward motion of the Pacific plate has been ~28° latitude since 70 Ma ago, but only ~10° since 30 Ma [*Beaman et al.*, 2007]. This indicates that during the Neogene, the environmental conditions related to geographic location for Shatsky Rise dredge sites should have changed little.

4. Samples and Methods

[11] Samples were selected from dredge hauls stored at Scripps Institution of Oceanography that

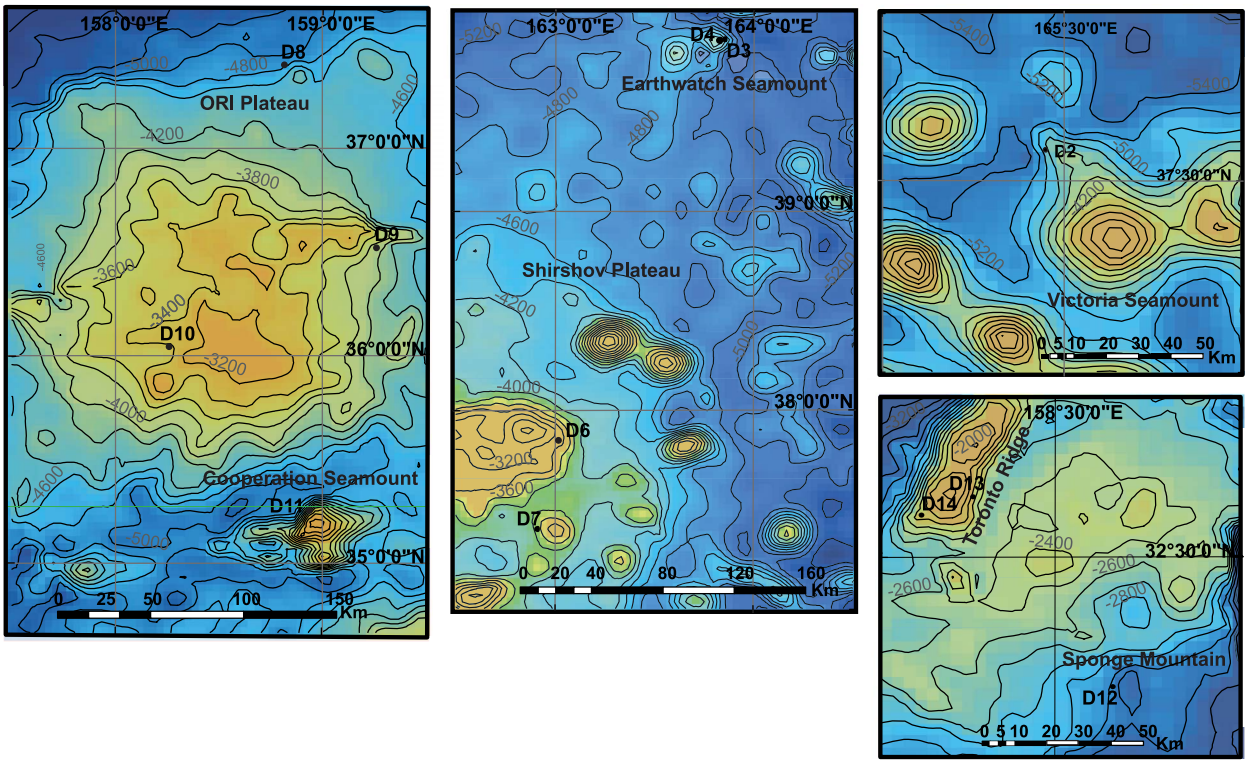

Figure 2. Bathymetric maps with detailed location of dredge sites shown in Figure 1.

were collected in 1994 during cruise TN037 aboard the R.V. *Thomas G. Thompson.* Dredges D12, D13, and D14 were collected on TAMU plateau: D13 and D14 are from the 1500 m-high Toronto ridge (900 m of which is buried beneath sediment) located on the northwest flank of TAMU, and D12 on a seamount called Sponge mountain, just south of the summit plateau (Figures 1 and 2 and Table 1). Dredge D11 was collected from Cooperation seamount, a twinned-peak basaltic volcano located within a basin that separates TAMU and ORI plateaus [*Sager et al.*, 1999]. Dredges D8–D10 were taken along the flanks of ORI plateau and D6 and D7 along the flanks of Shirshov plateau

Table 1. Location of Cruise TN037 Dredges Containing Analyzed Fe-Mn Deposits

Dredge	Latitude (N)	Longitude (E)	Water Depth (m)	Location	Max Crust Thickness[a] (mm)	Av Crust Thickness[a] (mm)	Substrate/Nucleus
D2	37°37.578′	165°27.519′	4833	N Victoria SM[b]	112	85	Breccia, CFA cement
–	–	–	–	–	58	50	Limestone nucleus
D3	39°51.914′	163°53.660′	4227	N Arm volcano	75	65	No substrate
–	–	–	–	–	59	56	No nucleus
D4	39°50.264′	163°54.789′	4000	Earthwatch SM	118	90	Breccia, CFA + Mn cement
D6	37°48.292′	163°07.521′	3835	E flank Shirshov	116	90	Nodule fragment nucleus
D7	37°23.500′	162°54.906′	3759	S flank Shirshov	136	110	No substrate
–	–	–	–	–	90	44	Nodule fragment nucleus
D8	37°23.604′	158°50.294′	4806	N flank ORI	10	5	Sandy claystone w/barite
–	–	–	–	–	82	72	Claystone nucleus
D9	36°31.150′	159°11.619′	3900	E flank ORI	55	30	Altered basalt, breccia
D10	36°08.070′	158°22.454′	3474	Central ORI	34	29	Breccia, phosphorite
D11	35°15.700′	158°57.050′	3760	Cooperation SM	68	60	Altered basalt, hyaloclastite
D12	32°12.927′	158°36.210′	3016	Sponge Mtn	40	29	Phosphorite, breccia
D13	32°43.366′	158°15.147′	2357	Toronto Ridge	37	22	Phosphorite, some Mn rich
D14	32°40.226′	158°04.866′	2155	Toronto Ridge	110	58	Phosphorite, breccia

[a]For nodules (dashes), maximum and minimum diameters are given.
[b]SM = seamount.

(Figures 1 and 2). Dredges D3 and D4 taken on seamounts (N Arm and Earthwatch) located just south of a trough that separates Shirshov plateau from Papanin Ridge. Dredge D2 was taken on the lower flank of one of the approximately 80 seamounts that constitute the Ojin Rise seamount province (Figures 1 and 2).

[12] X-ray diffraction mineralogy was completed using a Philips diffractometer with Cukα radiation and graphite monochromator. Semiquantitative mineral percentages were determined by using peak intensities and weighting factors relative to quartz set as 1 [*Cook et al.*, 1975; *Hein et al.*, 1988]. The detection limit for each mineral falls between about 0.2 and 1.0%, except for the manganese minerals, for which the limits are greater, probably as much as 10% for δ-MnO_2.

[13] Abundances of the 10 major oxides and Ba, Cr, Nb, Rb, Sr, Y, Zr, Th, and U in substrate rocks were determined by X-ray fluorescence spectrometry using a borate fused disk (XRF); Fe(II) by colorimetric titration; CO_2 by coulometric titration; H_2O^+ by water evolved at 925°C as determined coulometrically by Karl-Fischer titration; H_2O^- by sample weight difference after heating to 110°C for more than one hour; F and Cl by specific-ion electrode, S and C by combustion in an induction furnace and analysis of the generated SO_2 and CO_2 by infrared spectroscopy.

[14] For Fe-Mn crusts and nodules, the concentrations of the 10 major elements were determined by XRF on a borate fused disk representing the average composition of the entire crust sample; B, Ba, Cr, Cu, Li, Ni, Sr, V, Zn, and Zr were determined by inductively coupled plasma spectrometry (ICP) and Ag, As, Be, Bi, Br, Cd, Ce, Co, Ge, Hf, In, Mo, Nb, Pb, Rb, Sb, Sc, Se, Sn, Te, Th, Tl, U, W, and Y, by ICP-mass spectrometry using a 4-acid digest (ICP-MS); REEs by ICP-MS using a Li-metaborate fused disk; platinum group elements (PGEs: Ir, Pd, Pt, Rh, Ru) and Au by Ni-sulfide fire assay and ICP-MS; Te and Se were also determined by hydride generation and graphite furnace atomic-absorption spectrometry (AAS); Hg by cold vapor AAS; S by combustion and infrared spectroscopy; and Cl by specific-ion electrode. Analytical precision is better than 1.5% for all elements except Cl, which is better than 5.0%, and PGEs (better than 10%). Elements that have more than 30% of the values near or below the detection limit (in parentheses) include Cs (3 ppm), Se (5 ppm), Au (2 ppb), and Ir (2 ppb); elements with all values below detection limit are Ag (0.2 ppm), Ge (10 ppm), In (0.5 ppm), and Sn (2 ppm). Some crusts were split into two or more (up to 5) layers defined by well-developed textural differences. Bulk crust samples were also analyzed for those that were split into layers. All depths within Fe-Mn crusts are given in millimeters from the crust surface that was in contact with seawater.

[15] REE plots are normalized to both chondrites [*Anders and Grevesse*, 1989] and shale (PAAS, Post-Archean Australian Shale [*McLennan*, 1989]). The Ce anomaly was calculated as Ce* = 2Ce/(La + Pr) for PAAS-normalized values.

[16] Four subsamples forming a depth profile were taken from each of four select Fe-Mn crusts with a dentist drill to determine average growth rates and ages using the ratio between cosmogenic ^{10}Be and stable ^{9}Be. The ^{10}Be concentrations were determined by isotopic dilution using accelerator mass spectrometry (AMS). A precisely weighed amount of a ^{9}Be carrier was added to weighed aliquots of the sample powders and the samples were dissolved in 6 M HCl. The sample solutions were further purified and prepared for AMS analyses following a previously established method [*Frank et al.*, 1994]. The AMS measurements were performed at the 0.5 MV AMS facility "TANDY" [*Müller et al.*, 2010], ETH Zürich, Switzerland. The measured ^{10}Be/^{9}Be ratios were normalized to the secondary ETH Zürich S2007N with a nominal value of ^{10}Be/Be = 28.1×10^{-12} [*Kubik and Christl*, 2010]. The 1σ statistical uncertainties of the ^{10}Be measurements were between 3% and 5% taking into account both the counting statistics of the ^{10}Be "events" and the reproducibility of repeated measurements, which were performed for each sample, standard, and blank. The newly revised half-life of ^{10}Be of 1.387 Myr was applied [*Korschinek et al.*, 2010; *Chmeleff et al.*, 2010].

[17] The natural authigenic ^{9}Be concentration of the Fe-Mn crust samples was acquired at the ICPMS-Laboratory of the Institute of Geosciences, University of Kiel, using an AGILENT 7500cs ICP-MS instrument following established standard procedures [*Garbe-Schönberg*, 1993]. The measurements were performed on an aliquot of the same solution as used for ^{10}Be measurement in order to guarantee that the determined natural ^{10}Be/^{9}Be represents a true seawater ratio, which for the surface sample is consistent with the modern seawater ratio. For ratios deeper in the crusts, a seawater signal is indicated by a consistent decrease that follows an exponential decay, which means that the likelihood of a seawater signal is very high; in

addition, the REE patterns are typical for hydrogenetic crusts. Repeat measurements of samples processed separately through the leaching procedure indicate a 1σ reproducibility of 5%.

[18] The age of each crust below the upper 20 mm dated using Be isotopes was determined using an empirically derived cobalt chronometer method (growth rate GR = $0.68/(Co^n)^{1.67}$, where $Co^n = Co \times (50/Fe + Mn)$, with metals in wt. % [*Manheim and Lane-Bostwick*, 1988]), and by extrapolation of the deepest layer rate determined by Be isotope; the occurrence of growth hiatuses and changes in growth rates in the parts of the crusts not covered by $^{10}Be/^{9}Be$ data cannot be excluded (see *Frank et al.* [1999] for discussion). *Frank et al.* [1999] adjusted the empirical Co growth-rate relationship to match the available $^{10}Be/^{9}Be$ data and then used this adjusted relationship to extrapolate beyond the time covered by $^{10}Be/^{9}Be$ data. Here, we use the two techniques independently and so differences are to be expected.

[19] The Pearson correlation coefficient was used to calculate correlation coefficient matrices for the chemical data. Q-mode factor analysis was used to examine inter-element relationships and to identify common groups of elements referred to as factors. On the basis of X-ray diffraction mineralogy and element correlations, we interpret each factor to represent a particular mineral or phase in the Fe-Mn crusts and elements in that factor to be associated with or contained in that mineral or phase. This links mineralogy that reflects environmental conditions to element concentrations that in part reflect different sources. For Q-mode factor analysis, each variable percentage was scaled to the percent of the maximum value before the values were row-normalized and cosine-theta coefficients calculated. Factors were derived from orthogonal rotations of principal component eigenvectors using the Varimax method [*Klovan and Imbrie*, 1971]. All communalities, an index of the efficiency of a reduced set of factors to account for the original variance, are ≥0.90. Low factor scores between −0.18 and +0.18 were discarded because they are not statistically significant.

5. Results

[20] A wide variety of Fe-Mn morphological types were recovered during cruise TN037, including Fe-Mn-oxide pavement, Fe-Mn-oxide-coated cobbles, Fe-Mn nodules, and amalgamated crust-nodule deposits (Fe-Mn nodules cemented into pavements; Figure 3), which grade with depth into nodule conglomerate; the cement is Fe-Mn oxides, which also cement some breccia substrate rocks. In many dredge hauls, both crusts and nodules were collected indicating the close proximity of rock outcrops and sediment-covered seabed. Nodules generally have a small nucleus of an older nodule fragment, or less commonly a rock fragment (abyssal-type nodules [*Hein et al.*, 2000]). Deep-ocean amalgamated deposits have not been previously described and the close occurrence of crusts and abyssal-type nodules on seamounts and ridges is not common.

[21] Crusts for the most part are quite thick, but vary from 5 to 136 mm (Table 1); 260 mm is the thickest crust collected to date from the global ocean [*Hein et al.*, 2000]. The thickest Shatsky Rise crust was recovered from dredge haul D7 taken on the flank of Shirshov plateau. Thick crusts are layered, with columnar, massive, mottled, laminar, and/or botryoidal laminae, typical of hydrogenetic Fe-Mn crusts. Small rock and mineral fragments and isolated nodules occur within some crusts attesting to the dynamic seabed environment where the crusts formed. Surface textures of crusts are generally smooth, indicating current abrasion of surfaces that were once botryoidal. Carbonate ooze adhered to the surface of some nodules and red clay to some crusts during the dredging process.

[22] Fe-Mn crust substrate rock types also vary widely and include altered basalt, breccia, hyaloclastite, limestone, mudstone, and phosphorite composed of carbonate fluorapatite (CFA). Pure phosphorite is represented by replaced foraminiferal limestone and phosphatic rocks include CFA-cemented breccia and hyaloclastite and partly replaced reef limestone. These are typical substrate rocks for Fe-Mn crusts collected from seamounts elsewhere in the Pacific.

5.1. Composition of Selected Substrate Rocks

[23] Six representative substrate samples of fine-grained and altered rocks were selected and analyzed to determine their mineralogy and chemical composition (Table 2). Phosphorite is common in dredge hauls D12, D13, and D14. These are typical seamount-type deep-water phosphorites like those collected from many locations further south in the PCZ [*Hein et al.*, 1993]. These three dredge sites are the shallowest-water sites (Table 1) and the southernmost of those sampled during TN037. The other substrate rock samples analyzed are composed of volcanogenic minerals and their alteration products (Table 2), which are highly altered with high

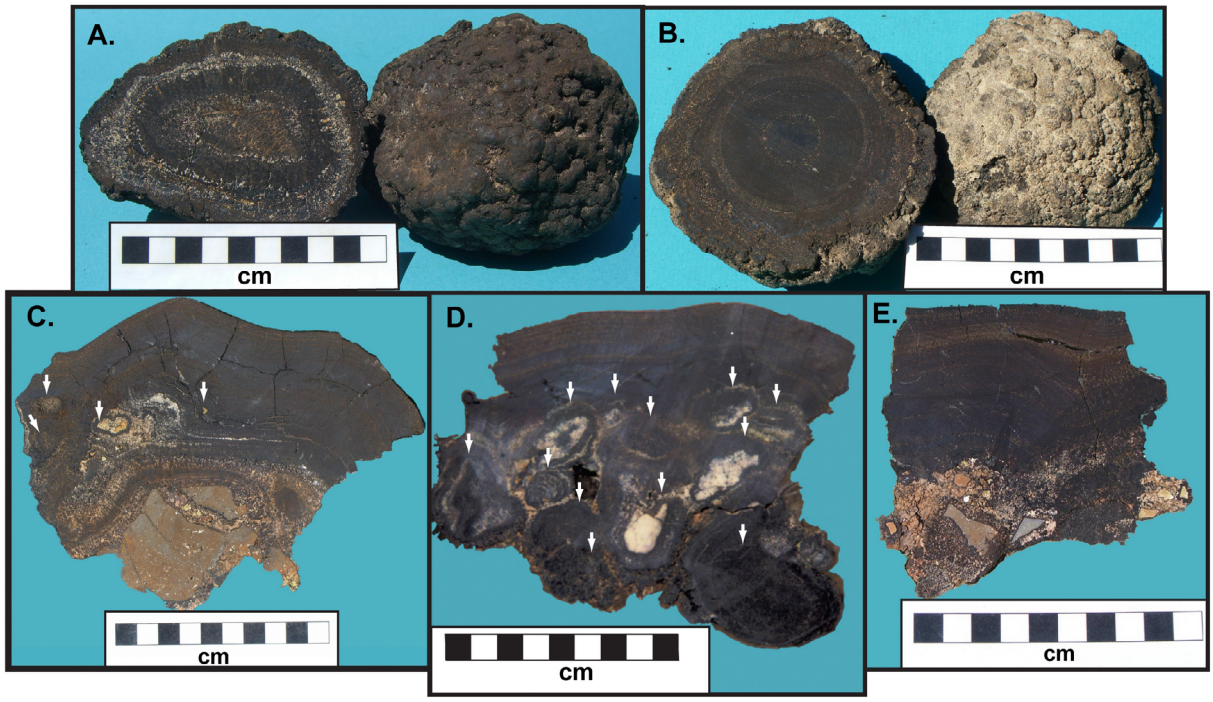

Figure 3. Photographs of a cross-section of Fe-Mn crusts, nodules, and amalgamated crust-nodule deposits. Arrows point out nodules that are overlain by Fe-Mn crust in two samples. (a) Fe-Mn nodule D7–1N showing the interior cut face and the exterior texture. (b) Fe-Mn nodule D6–1N. (c) Fe-Mn crust sample D4–1, 90–118 mm thick Fe-Mn crust with a few Fe-Mn nodules, indicated by white arrows, in the crust on a breccia substrate. (d) Sample D7–07 showing nodules, indicated by white arrows, in the lower portion of the crusts cemented with Fe-Mn oxides and overlain by a ~30 mm thick Fe-Mn crust. (e) Sample D2-03-02 is a 70–80 mm thick Fe-Mn crust with breccia substrate.

water contents and little to no reduced iron. Barite occurs in a sample of strongly sheared pinkish-brown claystone (D8–1A2). There is no indication of hydrothermal alteration of these rocks.

5.2. Fe-Mn Crust and Nodule Mineralogy

[24] All Fe-Mn samples are predominantly δ-MnO_2 (vernadite), which has only two X-ray reflections at about 2.42 Å and 1.41 Å. One crust layer may contain todorokite, but generally diagenetic and hydrothermal manganese minerals (7 and 10 Å manganates) are below the detection limit of about 5%. The δ-MnO_2 mineralogy of the Fe-Mn nodules indicates that they are also hydrogenetic without a significant diagenetic component. The main iron phase is X-ray amorphous. Accessory minerals include eolian quartz, plagioclase, and illite carried by westerly winds from Asia [*Leinen et al.*, 1994], and detrital plagioclase and smectite from local sources; there is no local source for quartz and illite. Some samples also contain phillipsite or amphibole. The innermost layer (69–97 mm, adjacent to substrate) of a thick crust from dredge haul D14 contains CFA, which is not found in any other TN037 Fe-Mn crust. The lower layers of thick crusts from more equatorial regions are commonly phosphatized [*Hein et al.*, 1993].

5.3. Fe-Mn Crust and Nodule Geochemistry

[25] Fifty-one samples were analyzed for chemical composition including 21 bulk crusts, 25 crust layers (2 of which are nodular layers), and 5 bulk nodules (Table 3). Chemical data are presented on a hygroscopic water-free basis (0% H_2O^-). The mean Fe/Mn ratio is 0.9 (range 0.5–2.0; Table 3), within the range of most hydrogenetic Fe-Mn crusts and only slightly higher than the 0.7 mean ratio of PCZ crusts. Si/Al ratios (mean 4.6) indicate that Si is enriched relative to Al in Fe-Mn crusts and nodules compared to substrate rocks. That excess silica most likely reflects biogenic silica and eolian quartz.

[26] Ni (max 0.84%), Co (max. 0.52%), and Cu (max. 0.50%) are the metals of greatest economic interest, along with Mn; individual nodule combined concentrations reach up to 1.33 wt. % (D6-1N-A) and individual crust layers up to 1.57%

Table 2. Chemical Composition of Select Fe-Mn Crust Substrate Rocks[a]

	D8-1A2	D9-12D	D10-11B	D12-2B2	D13-11A2	D13-15B2
SiO_2 (wt%)	49.9	47.6	47.3	3.66	1.30	10.1
Al_2O_3	15.7	17.4	14.9	0.66	0.39	4.53
FeO	<0.1	0.1	<0.1	<0.1	0.1	0.2
Fe_2O_3	6.79	14.5	14.0	0.37	1.28	11.9
MgO	4.06	1.77	4.58	0.30	0.34	1.19
CaO	1.72	4.97	1.01	51.1	52.3	29.5
Na_2O	1.65	2.97	1.84	0.84	0.67	1.06
K_2O	3.64	2.19	5.61	0.14	0.05	0.73
TiO_2	0.586	1.93	1.11	0.049	0.034	0.917
P_2O_5	0.88	0.25	0.53	31.3	32.1	19.1
MnO	1.87	0.25	0.79	0.02	0.77	8.49
LOI	8.52	3.60	5.45	10.7	3.30	10.3
Total	95.4	97.5	97.3	99.2	92.8	98.3
H_2O^+	6.8	3.6	6.4	1.9	2.5	6.2
H_2O^-	6.2	5.2	7.0	0.3	0.8	7.9
CO_2	0.16	0.02	0.07	4.87	5.18	2.67
C_{total}	–	–	–	1.58	–	–
S_{total}	–	–	–	0.67	–	–
F	–	–	–	2.97	–	–
Ba (ppm)	>10000	193	812	<20	<20	2390
Cl	–	–	–	871	–	–
Cr	<0.01	0.03	0.04	<0.01	<0.01	<0.01
Nb	3	8	3	<2	<2	2
Rb	115	37	71	<2	2	19
Sr	500	184	111	976	1120	1170
Y	169	36	63	233	937	822
Zr	226	108	187	27	28	186
Th	–	–	–	<2	–	–
U	–	–	–	5	–	–
CaO/P_2O_5	1.95	19.9	1.91	1.63	1.63	1.54
Rock type	claystone	basalt	basalt	phosphorite	phosphorite	breccia

[a]LOI = loss on ignition at 925° C. Dash = not analyzed.

(D4–1E) for those three metals, which are below the 2.0 wt.% commonly considered the potentially economic cut-off grade for nodules. The mean Cu content of the crusts analyzed here is about 300–400 ppm higher than regional means elsewhere in the global ocean although the mean Ni content falls within the range of large regional areas (Figure 4) [*Hein et al.*, 2000; *Hein and Koschinsky*, 2012]. The mean Cu/Co ratio is 0.65 for all samples, 0.63 for crust layers, 0.49 for bulk crusts, and 2.0 for the five bulk nodules (Tables 4–6). The high mean ratio for the nodules is identical to the mean ratio for the seven crust layers with high Cu concentrations (>0.20%). The same trend is noted for Ni/Co ratios, with bulk crust ratios averaging 1.3 and nodules 3.0. The highest Cu and Ni layers in crusts are always middle or lower layers, such as 46–68 mm for D3–1, 56–92 mm for D4–1, and 31–78 mm for D7–1. No near surface layers or thin crusts are strongly enriched in Cu (>0.20%) or Ni (>0.45%). For example, thin bulk crusts plus the thin outermost layer (<25 mm) of thicker crusts average 923 ppm Cu and 2755 ppm Ni, whereas crust layers below 30 mm average 2281 ppm Cu and 4705 ppm Ni. Lithium and especially Th are also strongly enriched in the same older crust layers as Cu and Ni and also compared to other crusts from open-ocean Pacific sites (Figure 4).

[27] Phosphorus averages about 0.54% for all the data combined, typical of most non-phosphatized Fe-Mn crusts. Only one crust (D14–16) is phosphatized and has 3.72% P in the lowermost layer (69–97 mm; Table 3); no nodules are phosphatized. The PGEs are generally low compared to PCZ samples; bulk crust D14–16B has the highest concentrations of PGEs, with 689 ppb Pt. Hg is very high (69–97 ppb) in five samples as is Au (54–66 ppb) compared to PCZ samples, which

Table 3 (Sample). Hygroscopic Water-Free (0% H_2O^-) Composition of Fe-Mn Crusts, Crust Layers in mm From Crust Surface, and Nodules[a] [The full Table 3 is available in the HTML version of this article]

	D2-3-1A	D2-3-1B	D2-3-1C	D2-3-1D	D2-3-2A	D2-3N-A	D3-1A	D3-1B	D3-1C	D3-2N-A	D4-1A
Fe (wt%)	21.6	24.4	22.6	19.8	23.4	20.6	14.0	17.7	19.7	20.4	26.8
Mn	23.9	21.1	28.8	29.3	28.9	20.6	22.8	21.4	25.1	22.7	24.4
Fe/Mn	0.9	1.2	0.8	0.7	0.8	1.0	0.6	0.8	0.8	0.9	1.1
Si	9.20	10.5	7.54	8.34	8.78	11.3	15.9	15.3	11.0	11.5	8.83
Al	2.45	2.05	1.63	2.10	1.86	2.40	2.65	2.55	2.07	1.84	2.26
Na	1.75	1.72	1.87	1.76	1.88	1.84	2.17	2.32	1.88	2.04	1.61
K	0.93	0.94	0.82	0.73	0.96	1.02	1.35	1.11	1.20	0.99	1.18
Mg	1.49	1.45	1.57	1.71	1.62	1.45	2.07	1.60	2.05	1.50	1.66
Ca	2.46	2.11	2.64	2.91	2.65	1.94	1.70	1.91	1.97	1.96	2.41
Ti	1.17	0.967	1.36	1.38	1.34	0.917	0.424	0.534	0.661	0.761	1.51
P	0.41	0.42	0.41	0.39	0.42	0.32	0.17	0.26	0.27	0.28	0.46
S	0.14	0.12	0.14	0.11	0.09	0.07	0.09	0.11	0.10	0.08	0.15
Cl	1.01	1.01	1.12	1.21	0.991	0.956	0.909	1.07	1.12	0.942	0.689
As (ppm)	206	244	225	185	215	175	89	131	139	141	225
B	654	639	632	348	547	217	289	265	537	251	465
Ba	1681	1616	1877	2032	1904	1417	3848	1631	3233	1618	2352
Be	11	30	9.9	9.5	8.4	7.4	4.4	5.6	6.7	6.6	11
Bi	39	24	38	44	37	20	10	12	19	22	35
Br	24	24	25	25	21	22	22	25	23	22	17
Cd	4.3	3.5	4.0	5.2	4.0	3.9	8.8	5.9	7.1	5.4	4.2
Co	2365	1821	2872	3579	2915	2125	1263	1312	1599	1618	2121
Cr	23	34	13	42	13	7	7	61	25	62	37
Cu	1144	748	1220	1808	1188	1429	3836	2305	3257	2289	1517
Hf	4	<1	3	7	1	2	5	4	10	3	5
Li	7	6	6	9	5	15	21	18	25	18	8
Mo	537	604	662	650	662	440	442	392	499	342	591
Nb	62	47	65	77	67	44	13	20	29	30	60
Ni	2365	1749	2720	3616	2759	2695	5801	4551	5325	4358	2404
Pb	1273	1327	1537	1259	1503	1359	744	1061	1202	1445	1607
Rb	23	23	13	9	14	20	32	24	23	20	15
Sb	35	40	38	34	38	33	28	32	44	39	54
Sc	11	12	10	11	11	14	19	15	15	14	18
Se	<5	19	40	<5	25	19	16	17	<5	8	13
Sr	1261	1291	1474	1372	1438	1196	895	998	1165	1237	1491
Te	22	13	22	37	26	16	4.6	6.1	8.9	11	44
Th	127	114	152	128	148	113	29	41	48	10	68
Tl	131	86	132	160	135	117	74	59	80	70	104
U	9.5	12	16	10	11	11	5.4	6.7	4.3	9.7	11
V	681	706	670	574	588	504	335	417	459	461	672
W	65	69	72	79	70	45	34	30	49	30	62
Zn	485	485	520	605	567	602	908	788	846	837	648
Zr	685	669	678	756	699	560	457	498	614	543	752
Au (ppb)	36	12	57	31	40	<2	44	58	12	6	36
Hg	14	25	14	15	12	74	29	31	29	53	10
Ir	5	2	3	5	–	–	–	–	–	2	5
Pd	5	5	8	7	–	–	9	–	–	7	8
Pt	150	75	136	287	–	–	124	–	–	127	366
Rh	13	8	14	21	–	–	6	–	–	8	22
Ru	12	10	13	15	–	–	7	–	–	9	13
Interval	0–112	0–37	37–82	82–112	0–70	0–54	0–68	0–46	46–68	0–57	0–118
Type	bulk	layer	layer	layer	bulk	nodule	bulk	layer	layer	nodule	bulk

[a]Dash = not analyzed.

may indicate a hydrothermal component in Shatsky Fe-Mn crusts [*Hein et al.*, 2005].

[28] Two or more layers were analyzed for eight Fe-Mn crusts. Fe, Mn, and their respective associated elements (see below) increase, and the aluminosilicate-associated elements decrease in the lower layer of the two layers of crusts D3–1 and D9–12. Mn, Mn-associated elements, and PGEs generally decrease from the substrate to the crust surface for crusts D2–3 (112 mm thick) and D11–2 (68 mm

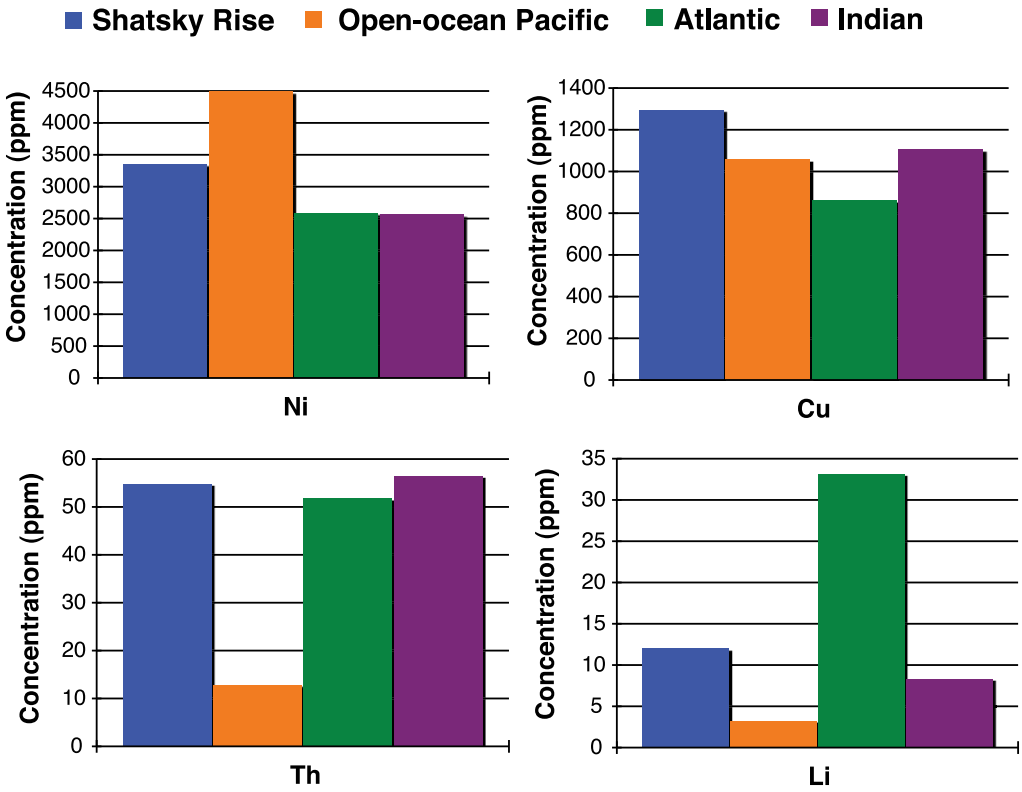

Figure 4. Comparison of Shatsky Rise mean bulk Fe-Mn crust composition for selected elements with mean crust values for Atlantic, Indian, and open-ocean Pacific crusts.

thick; 3 layers each), whereas Fe and associated elements show the opposite trend. In contrast, most elements show uniform concentrations through the three layers of the relatively thin crust D10–11 (25 mm thick). The other Fe-Mn crusts show more complex patterns determined by the anomalous composition of one of the layers; for example, layer 4 of the 5 in sample D4–1 (118 mm) is high in aluminosilicate elements and very low in Fe and layer 5 is also high in aluminosilicate elements, but very low in Mn, consequently, other elements either increase toward or away from those layers. The phosphatized layer (lowermost of 4 layers) in crust D14–16 (110 mm thick) is another example of an anomalous layer.

[29] A ternary plot of Fe:Mn:(Co + Ni + Cu) × 10 shows that about half the sample data fall within the lower part of the open-ocean hydrogenetic crust field (field B in Figure 5). The remainder of the data in the ternary plot trend toward the hydrothermal field (field C in Figure 5) or fall between the hydrogenetic and diagenetic fields (field A in Figure 5).

5.4. Yttrium and Rare Earth Elements

[30] Total REEs plus Y range from very high (0.51%; crust D2-3-1A; 7.5% are heavy REEs) to quite low (0.081%; crust D3–1A; 17.6% are heavy REEs), with Ce concentrations up to 0.43% (crust layer D2-3-1D; Table 7). Only Ce among the REEs is higher in Shatsky Rise samples compared to PCZ samples. Yttrium and the REEs decrease in the upper layer of the two layers of crusts D3–1 and D9–12. The REEs increase (except Ce which decreases) from the substrate to the crust surface for crusts D2–3 (3 layers) and D11–2 (3 layers). In contrast, the REEs increase from the bottom and surface layers to the central layer through the three layers of sample D7–1C and sample D10–11, except Ce in D10, which shows the opposite trend. The other crusts show more complex patterns determined by the anomalous composition of one of the layers; for example, layer 4 of the 5 layers of sample D4–1 is high in aluminosilicate elements and very low in Fe, consequently, the REEs increase away from that layer and also decrease from layer 2 to the top layer, which has the highest concentrations for that crust, except for Ce. In four-layer crust

Table 4. Statistics for 51 Bulk Fe-Mn Crusts, Crust Layers, and Nodules (Data From Table 3)

	N	Mean	Median	SD[a]	Min[b]	Max[c]
Fe (wt. %)	51	22.1	22.9	4.28	12.2	28.3
Mn	51	25.0	24.7	4.69	7.84	35.8
Fe/Mn	51	0.9	0.9	0.9	1.5	0.8
Si	51	9.51	9.00	3.08	4.55	20.1
Na	51	1.92	1.88	0.22	1.56	2.96
Mg	51	1.64	1.60	0.23	1.12	2.28
Al	51	2.05	1.88	0.87	0.72	5.20
P	51	0.54	0.43	0.54	0.16	3.72
K	51	1.02	0.94	0.36	0.61	2.47
Ca	51	2.62	2.33	1.39	1.34	10.2
Ti	51	1.001	0.942	0.316	0.424	1.938
S	51	0.14	0.14	0.05	0.05	0.28
LOI	51	20.5	20.6	2.73	13.5	26.1
As (ppm)	51	200	206	66	56	334
B	51	347	271	169	140	818
Ba	51	2469	2005	1315	1417	9214
Be	51	7.5	7.0	3.7	2.9	29.8
Bi	51	33.3	30.2	16.4	8.8	82.8
Br	51	24	23	8	13	59
Cl	51	10321	10133	3059	3741	24916
Co	51	2441	2121	1056	549	5186
Cr	51	37	39	21	5	82
Cu	51	1591	1220	1098	318	4983
Ga	51	14	14	5	8	35
Li	51	15	9	14	1	70
Mo	51	534	537	165	67	858
Nb	51	42	40	16	13	77
Ni	51	3625	3425	1612	840	8417
Pb	51	1602	1596	486	721	2677
Rb	51	19	18	8	5	44
Sb	51	43.3	44.4	9.2	10.4	65.2
Sc	51	12.0	11.1	4.1	4.6	27.5
Sr	51	1454	1472	324	705	1959
Te	51	25.0	20.3	17.6	3.1	74.9
Th	51	55.8	45.8	31.3	10.2	152
Tl	51	91.3	82.8	57.9	16.7	285
U	51	10.7	10.88	3.86	2.7	21.7
V	51	539	549	130	251	771
W	51	57	57	19	9	94
Y	51	178	169	83	76	561
Zn	51	699	687	141	332	999
Zr	51	598	613	101	386	850
Au (ppb)	51	~23	~19	18	<2	66
Hg	51	34	31	22	6	97
Ir	13	5	5	4	2	15
Pd	18	7	8	2	4	10
Pt	18	225	159	162	75	689
Rh	18	14	12	9	6	41
Ru	18	12	12	3	7	20
Depth (m)	51	3639	3760	815	2155	4833
Thickness[d]	51	40	27	33	4	136

[a]Standard deviation.
[b]Minimum.
[c]Maximum.
[d]Crust thickness in millimeters.

Table 5. Statistics for 21 Bulk Fe-Mn Crusts (Data From Table 3)

	N	Mean	Median	SD[a]	Min[b]	Max[c]
Fe (wt. %)	21	22.5	22.9	3.69	14.0	26.8
Mn	21	24.3	24.4	4.95	7.84	31.3
Fe/Mn	21	0.9	0.9	0.7	1.8	0.9
Si	21	9.52	8.83	3.48	4.85	20.1
Na	21	1.93	1.86	0.29	1.56	2.96
Mg	21	1.61	1.53	0.22	1.12	2.07
Al	21	1.98	1.86	0.93	0.87	5.20
P	21	0.54	0.46	0.43	0.17	2.35
K	21	0.98	0.93	0.26	0.62	1.48
Ca	21	2.59	2.41	1.18	1.34	7.44
Ti	21	0.997	0.962	0.285	0.424	1.508
S	21	0.15	0.14	0.05	0.08	0.27
LOI	21	20.3	21.0	2.90	13.5	24.5
As (ppm)	21	208	212	60	86	320
B	21	320	238	158	169	654
Ba	21	2604	1955	1692	1418	9214
Be	21	6.9	6.9	1.9	2.9	11.3
Bi	21	32.7	33.9	14.1	8.8	59.2
Br	21	25	23	10	16	59
Cl	21	11064	10060	3879	6179	24916
Co	21	2667	2576	1095	549	4988
Cr	21	33	32	20	5	82
Cu	21	1294	1181	779	399	3836
Ga	21	13	11	4	8	21
Li	21	12	8	10	3	37
Mo	21	523	537	166	67	787
Nb	21	43	43	14	13	67
Ni	21	3346	3203	1357	840	5801
Pb	21	1726	1694	546	721	2677
Rb	21	19	17	9	5	39
Sb	21	43.1	46.0	10.7	10.4	57.0
Sc	21	11.7	10.9	3.8	5.7	19.3
Sr	21	1526	1609	348	705	1944
Te	21	25.1	24.2	13.2	3.1	54.7
Th	21	54.8	46.9	30.2	22.3	148
Tl	21	80.0	80.6	45.2	20.8	180
U	21	10.8	10.9	3.0	4.5	16.3
V	21	545	559	125	251	726
W	21	55	54	17	9	87
Y	21	176	171	82	76	468
Zn	21	680	684	148	332	973
Zr	21	603	629	97	396	752
Au (ppb)	21	~23	~22	15	<2	44
Hg	21	38	38	24	10	97
Ir	7	5	5	5	2	15
Pd	10	7	8	2	4	10
Pt	10	232	165	177	97	689
Rh	10	14	12	10	6	41
Ru	10	11	12	4	7	20
Thickness[d]	21	48	35	40	5	136

[a]Standard deviation.
[b]Minimum.
[c]Maximum.
[d]Crust thickness in millimeters.

Table 6. Statistics for 25 Fe-Mn Crust Layers (Data From Table 3)

	N	Mean	Median	SD[a]	Min[b]	Max[c]
Fe (wt. %)	25	22.8	24.1	4.37	12.2	28.3
Mn	25	25.8	25.0	4.77	18.4	35.8
Fe/Mn	25	0.9	1.0	0.9	0.7	0.8
Si	25	8.97	8.37	2.78	4.55	15.3
Na	25	1.90	1.88	0.17	1.66	2.32
Mg	25	1.65	1.60	0.23	1.41	2.28
Al	25	2.00	1.88	0.84	0.72	4.26
P	25	0.59	0.48	0.66	0.26	3.72
K	25	1.01	0.88	0.41	0.61	2.47
Ca	25	2.80	2.37	1.64	1.61	10.2
Ti	25	1.053	0.967	0.349	0.494	1.938
S	25	0.15	0.14	0.04	0.06	0.28
LOI	25	21.2	20.7	2.53	16.4	26.1
As (ppm)	25	212	207	61	84	334
B	25	401	415	171	173	818
Ba	25	2348	2005	956	1463	5425
Be	25	8.3	7.3	4.8	3.0	29.8
Bi	25	36.4	30.2	18.7	11.5	82.8
Br	25	23	24	5	15	37
Cl	25	10090	10608	2318	3741	15588
Co	25	2419	2046	1044	1311	5186
Cr	25	43	42	20	8	75
Cu	25	1522	1220	1034	318	4837
Ga	25	15	14	6	8	35
Li	25	12	8	11	1	46
Mo	25	590	615	132	373	858
Nb	25	44	44	18	20	77
Ni	25	3628	3537	1762	1387	8417
Pb	25	1594	1596	416	749	2655
Rb	25	18	17	8	5	44
Sb	25	44.1	44.3	8.6	29.1	65.2
Sc	25	12.0	11.1	4.7	4.6	27.5
Sr	25	1473	1474	273	783	1959
Te	25	27.4	17.6	21.4	6.1	74.9
Th	25	56.6	45.8	31.7	11.8	152
Tl	25	108	93.5	66.5	16.7	285
U	25	11.5	11.5	4.1	2.9	21.7
V	25	562	554	128	253	771
W	25	63	64	18	30	94
Y	25	192	179	87	100	561
Zn	25	691	677	125	485	961
Zr	25	609	613	108	386	850
Au (ppb)	25	~26	~23	21	<2	66
Hg	25	27	24	19	6	69
Ir	5	5	5	2	2	8
Pd	6	7	8	1	5	8
Pt	6	222	165	163	75	520
Rh	6	15	14	8	7	27
Ru	6	13	13	2	10	16
Thickness[d]	25	25	19	17	4	83

[a]Standard deviation.
[b]Minimum.
[c]Maximum.
[d]Crust thickness in millimeters.

D14–16, the REEs increase away from layer 3, except Ce, which decreases.

[31] Normalized REE plots show patterns typical of hydrogenetic crusts and nodules: PAAS-normalized data show a positive Ce anomaly (Ce*) and convex up middle REE pattern (Figure 6). Chondrite-normalized patterns show a positive Ce anomaly, small positive Gd anomaly, LREE enrichment, and a progressive decrease in normalized HREE with increasing atomic number.

[32] The Ce* ranges from a very strong to a weak positive anomaly (11.5 to 1.7, respectively). In most samples, Ce* decreases in magnitude with distance from the substrate (decreasing age) in the crust, in other samples adjacent layers have similar values. Good examples are crusts D2-3-1 where Ce* decreases with time from 11.5 to 5.9 to 2.8 through three layers, and crust D11–2B decreases with time from 8.1 to 4.0 to 2.3 through three layers. There is a reversal in layer 3 of the oldest crust (D14–16B), where Ce* increases from 3.0 to 7.6, then decreases to 4.4 and then 3.0 for the uppermost layer (Table 6).

5.5. Inter-element Relationships and Grouping of Elements

[33] Correlation coefficient matrices were constructed for the chemical compositions of all data, bulk crusts, and crust layers. In addition to chemical elements, all matrices included longitude, latitude, water depth, and crust thickness.

[34] For the 21 bulk crust samples analyzed, statistically significant positive correlations ($p = 0.01$) are found among the following elements, which are assumed to represent the Mn, Fe, aluminosilicate, and CFA or biogenic phases: **Mn:** Mo, W, Sb, Bi, Co, Sr, U, Te, Pb, and V (at $p = 0.05$ also Ni, Nb,

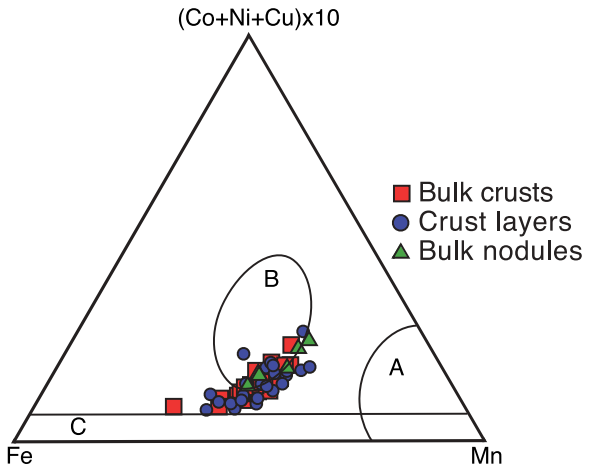

Figure 5. Ternary diagram of Fe:Mn:(Co+Ni+Cu)×10 for Shatsky Rise samples; field A is diagenetic, B hydrogenetic, and C hydrothermal.

Table 7 (Sample). Concentrations of Yttrium and Rare Earth Elements (ppm) in Fe-Mn Crusts [The full Table 7 is available in the HTML version of this article]

	D2-3-1A	D2-3-1B	D2-3-1C	D2-3-1D	D2-3-2A	D2-3N-A	D3-1A	D3-1B	D3-1C	D3-2N-A	D4-1A
Y	160	168	130	103	123	135	65	88	103	105	143
La	301	308	247	185	231	233	90.3	123	200	185	250
Ce	3930	1780	3030	4340	2640	1370	468	580	878	905	1750
Pr	68.6	72.6	58.6	41.4	54.3	56.3	22.5	29.6	46.7	43.2	54.1
Nd	305	331	259	180	242	259	110	144	220	202	248
Sm	69.8	75.2	59.5	40.5	54.8	59.3	25.8	33.1	49.8	45.6	55.2
Eu	15.9	17.3	13.4	9.11	12.5	13.8	6.02	7.78	11.7	10.7	12.6
Gd	74.7	77.5	62.3	46.1	58.4	61.8	28.1	35.9	52.9	48.9	59.2
Tb	9.7	10.5	8.1	5.8	7.6	8.4	3.8	5.0	7.1	6.6	7.7
Dy	54.8	59.3	45.4	32.8	43.0	47.5	22.6	29.0	39.8	37.8	44.7
Ho	8.97	9.51	7.36	5.54	7.08	7.70	3.74	4.83	6.36	6.09	7.33
Er	26.8	27.8	22.2	17.0	20.9	22.8	11.2	14.4	18.8	18.2	22.2
Tm	3.4	3.4	2.8	2.3	2.7	2.9	1.4	1.8	2.4	2.3	2.8
Yb	23.7	23.4	19.5	15.9	18.4	19.6	9.8	12.6	16.3	15.6	19.5
Lu	3.28	3.16	2.62	2.23	2.51	2.69	1.33	1.71	2.21	2.09	2.67
∑REE	4896	2799	3838	4924	3395	2165	805	1023	1552	1529	2536
Ce*[a]	6.4	2.8	5.9	11.5	5.5	2.8	2.4	2.3	2.1	2.4	3.5
Interval[b]	B 0–112	L 0–37	L 37–82	L 83–112	B 0–70	N 0–54	B 0–68	L 0–46	L 46–68	N 0–57	B 0–118

[a]Ce* = 2Ce/La + Pr from chondrite-normalized data.
[b]B = bulk, L = layer, CCB = coated cobble bulk.

Zn); **Fe:** As, U, V, Pb, Sr, Sb, Zr, and W; **Si:** Al, K, Rb, Na, and Sc (at p = 0.05 also Mg); **P:** Ca, Y, S, Cr, Te, Bi, Se, Ir, Pt, Rh, and Ru (at p = 0.05 also Tl). Copper shows a negative correlation with Fe and associated elements, but does not correlate with Mn; Cu has positive correlations with Ga, Mg, Ni, Cd, Ba, K, and Zn (at p = 0.05 also Au, Li, Rb). Nickel also has a negative correlation with Fe and associated elements, but unlike Cu, has a positive correlation with Mn as well as Cd, Zn, Cu, Mg, Ba, and Ga (at p = 0.05 also Li). Thorium does not correlate with any of the major phases and has positive correlations with Ta, B, Nb, and Be. Water depth has positive correlations with Latitude, Longitude, and Th at p = 0.01 and Si, Al, B, and Sc at p = 0.05; and negative correlations with Co, Sb, Pb, Sr, Zn, P, and Te, which indicates that Th and the aluminosilicate elements increase in crusts with increasing water depth, whereas some of the elements associated with the Mn, Fe, and CFA phases decrease with increasing water depth. These same relationships occur with increasing latitude, which stands to reason since water depth increases with increasing latitude. Rh, Tl, Ba, B, and Ga increase with increasing crust thickness and crust thickness increases with increasing longitude; Hg decreases with increasing crust thickness.

[35] Q-mode factor analysis for the bulk crust data set shows three factors that account for 96% of the variance and represent the Fe, aluminosilicate, and Mn phases (57%, 15%, and 23% of the variance respectively); a CFA/biogenic factor was not identified using Q-mode analysis. In addition to the elements listed above, the **Fe factor** has: REEs (except Ce), Ti, Bi, Mo, and Te; the **aluminosilicate factor** has Hg, Th, and Pd; and the **Mn factor** has: Ce, Li, Cu, Mg, Ba, Ga, and K, but does not have U, V, Nb, and As, all of which correlate with Mn; we assume that these latter elements are in a phase that covaries with the Mn phase which explains the correlations yet exclusion from the Q-mode Mn factor. If the one bulk crust with CFA in it is removed, then the elements that correlate in that phase are distributed in either the Fe (P, Ca) or Mn (PGEs) factors, otherwise they are not in any of the factors.

5.6. Growth Rates and Ages

[36] Growth rates of the upper 20 mm of the four crusts dated using $^{10}Be/^{9}Be$ vary from 10.5 mm/Myr to 2.1 mm/Myr (Figure 7 and Table 8). The three deeper-water crusts (3759–4000 m) generally have higher growth rates (10.5–3.1) than the shallower-water (2155 m) crust (2.1–3.7 mm/Ma). This is consistent with the higher oxidation potential for the deeper water compared to the oxygen minimum zone (OMZ) where the shallower-water crust formed.

[37] The base of the upper 20 mm of the four Be-isotope dated crusts ranges in age from 2.67 to 6.57 Ma, the shallow-water crust is the oldest. The earliest initiation of crust growth was approximately at 28 Ma for D14–16B based on the Co

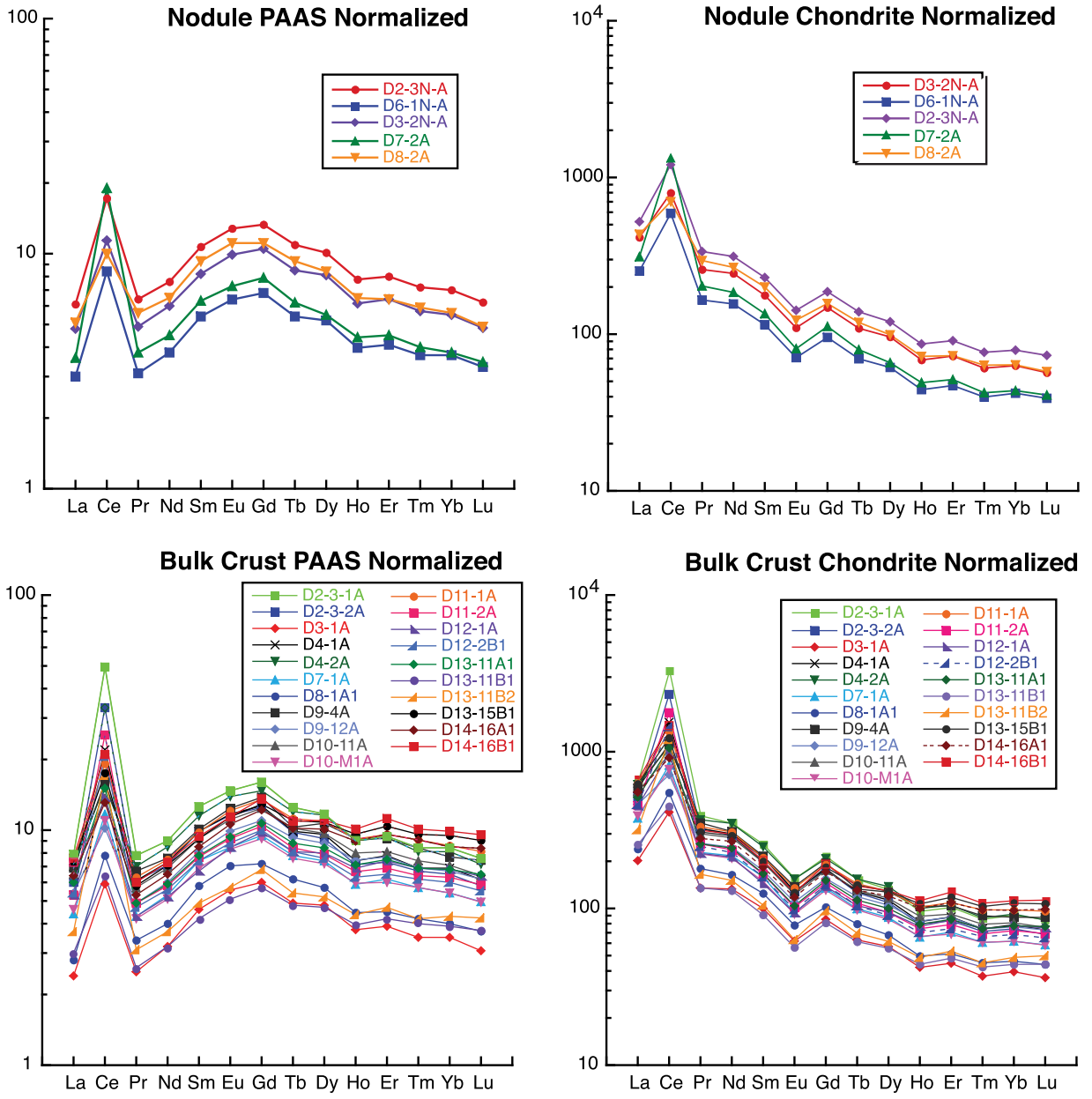

Figure 6. PAAS-normalized and chondrite-normalized rare earth element plots for bulk nodule and bulk crust samples.

chronometer, which is in good agreement with the 30 Ma extrapolated Be isotope age. Crust D11–2 began its growth 14.5 Ma ago based on the Co chronometer, which is in reasonable agreement with an extrapolated Be isotope age of 12.6 Ma. Crust D7–1 consists of a nodule conglomerate from the base at 130 mm to 30 mm, which is overlain by typical parallel laminae for the upper 30 mm. The depth at 30 mm corresponds to 3.5 Ma based on Co chronometer (4.4 Ma extrapolated Be age). Ages for the conglomerate layer are probably meaningless because the nodules may be of different ages and the ferromanganese cement may have formed rather rapidly. However, the Co chronometer would put the age at 78 mm, the extent of chemical data, at 8.2 Ma, which is very different from the extrapolated Be age of 12.5 Ma. Crust D4–1 shows significantly different ages of initiation of growth based on the Co chronometer (13.7 Ma) and extrapolated Be age (37.8 Ma), even when the surface sample is corrected to modern seawater Be isotope value (Tables 8 and 9). Why these ages for D4–1 are so different is unclear, but all of the Be-isotope ages are extrapolated whereas measured Co, Fe, and Mn

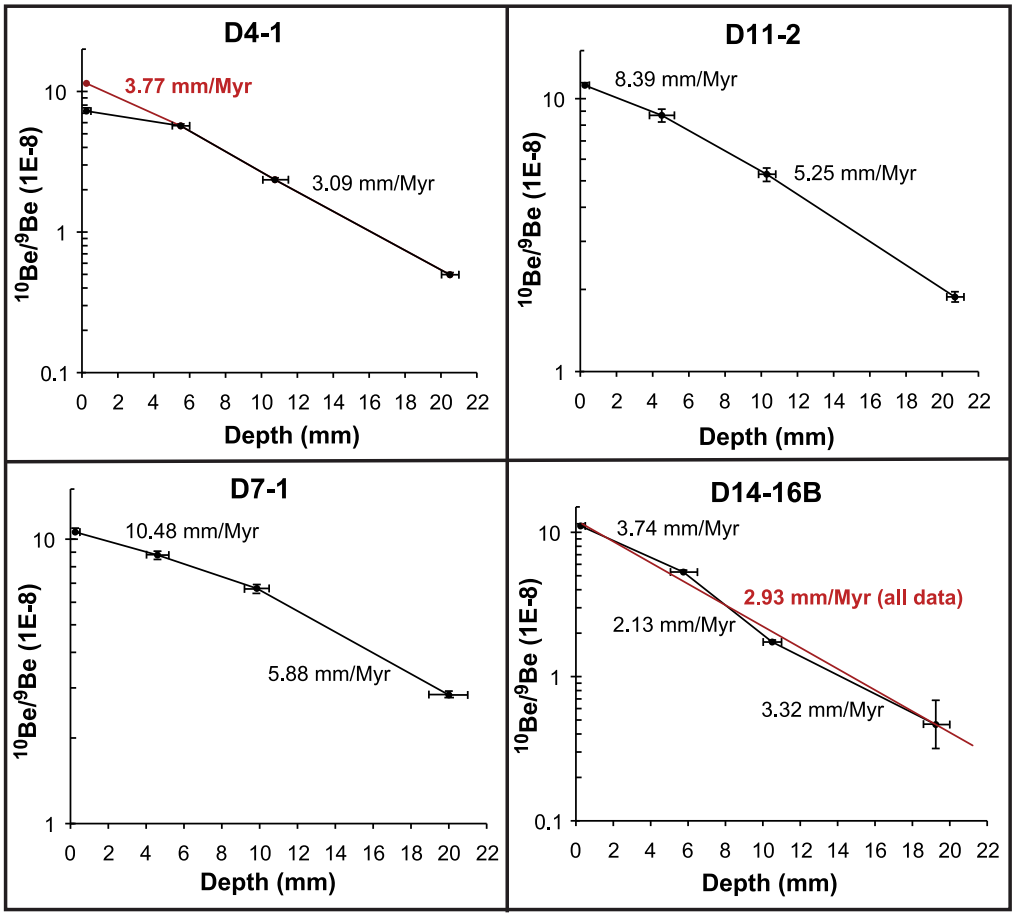

Figure 7. Growth-rate curves based on $^{10}Be/^{9}Be$ ratios; depth is from the crust surface that was in contact with seawater. The surface isotopic ratio for TN037-D4-1 is significantly lower than the other three crusts, which reflect contemporary seawater, possibly because of erosion of the surface; using the mean of the surface values for the other three crusts produces a nearly linear growth rate for D4–1. The red line for D14–16B is for a linear age model.

Table 8. Be Isotope Ages of Four Crusts From Cruise TN037

Sample	Mean Depth (mm)	^{10}Be (at./g (1e^{7}))	^{9}Be (ppm/error)	^{9}Be Conc (10^{16} at/g)	$^{10/9}Be$ ($\times 10^{-8}$)	Age (Ma)
D4-1-05	0.25 ± 0.25	327 ± 17	0.68/0.01	4.51 ± 0.05	7.256 ± 0.392[a]	0.91
D4-1-6	5.50 ± 0.50	1543 ± 47	4.06/0.04	27.12 ± 0.30	5.692 ± 0.183	1.39
D4-1-115	10.75 ± 0.75	763 ± 23	4.85/0.05	32.38 ± 0.36	2.356 ± 0.076	3.10
D4-1-21	20.50 ± 0.50	183 ± 6	5.52/0.06	36.85 ± 0.41	0.497 ± 0.018	6.26
D7-1-05	0.25 ± 0.25	1030 ± 32	1.46/0.02	9.73 ± 0.11	10.591 ± 0.345	0.02
D7-1-52	4.60 ± 0.60	2008 ± 61	3.42/0.04	22.83 ± 0.25	8.793 ± 0.282	0.44
D7-1-105	9.85 ± 0.65	1371 ± 41	3.06/0.03	20.43 ± 0.22	6.711 ± 0.216	0.94
D7-1-21	20.00 ± 1.0	533 ± 16	2.81/0.03	18.80 ± 0.21	2.833 ± 0.091	2.67
D11-2-05	0.25 ± 0.25	918 ± 29	1.23/0.01	8.20 ± 0.09	11.193 ± 0.378	0.03
D11-2-52	4.50 ± 0.70	1930 ± 58	3.33/0.04	22.22 ± 0.24	8.688 ± 0.279	0.54
D11-2-108	10.30 ± 0.50	1606 ± 48	4.55/0.05	30.39 ± 0.33	5.286 ± 0.170	1.64
D11-2-202	20.70 ± 0.50	601 ± 18	4.79/0.05	32.03 ± 0.35	1.877 ± 0.060	3.62
D14-16B-05	0.25 ± 0.25	1722 ± 57	2.33/0.03	15.56 ± 0.17	11.068 ± 0.389	0.09
D14-16B-65	5.75 ± 0.75	1298 ± 39	3.66/0.04	24.48 ± 0.27	5.301 ± 0.171	1.96
D14-16B-110	10.50 ± 0.50	391 ± 12	3.37/0.04	22.51 ± 0.25	1.736 ± 0.057	3.58
D14-16B-200	19.25 ± 0.75	122 ± 6	3.94/0.04	26.31 ± 0.29	0.465 ± 0.022	6.57

[a]The measured surface $^{10/9}Be$ ratio is too low for modern Pacific seawater and the upper 0.8 Ma of crust is likely missing; the ages given assume 11.42×10^{-8} to be the correct surface value (average of other 3 samples).

Table 9. Age of Cu Enrichment in Crusts From NE to SW Along Shatsky Rise Compared to Non-enriched Crusts (D9, D10, D11?)[a]

Sample and Interval (mm)	Cu (ppm)	Ni (ppm)	Li (ppm)	Age of Boundaries (Ma)	Dating Method[b]	Water Depth (m)
D2-3-1B 0-37	748	1749	6	0–3.7	Co	4833
D2-3-1C 37-82	1220	2720	6	3.7–11.6	Co	
D2-3-1D 82-112	**1808**[c]	**3616**	**9**	**11.6–19.8**	Co	
D3-1B 0-46	2305	4551	18	0.0–3.4	Co	4227
D3-1C 46-68	**3257**	**5325**	**25**	**3.4–4.4**	Co	
D4-1B 0-26	652	1553	5	0–8.0	$^{10/9}$Be (ext)	4000
				0–2.2	Co	
D4-1C 26-42	699	2700	1	8.0–13.2	$^{10/9}$Be (ext)	
				2.2–3.4	Co	
D4-1D 42-56	**2270**	**5791**	9	**13.2–17.7**	$^{10/9}$Be (ext)	
				3.4–4.7	Co	
D4-1E 56-92	**4837**	**8417**	**46**	**17.7–29.4**	$^{10/9}$Be (ext)	
				4.7–10.8	Co	
D4-1F 92-118	1735	1810	12	29.4–37.8	$^{10/9}$Be (ext)	
				10.8–13.7	Co	
D7-1B 0-15	958	2111	7	0–1.8	$^{10/9}$Be	3759
				0–1.1	Co	
D7-1C 15-30	1500	3388	10	1.8–4.4	$^{10/9}$Be (ext)	
				1.1–3.5	Co	
D7-1D 30-78	**3418**	**7217**	**40**	**4.4–12.5**	$^{10/9}$Be (ext)	
				3.5–8.2	Co	
D9-12B 0-20	681	1387	8	0–1.2	Co	3900
D9-12C 20-38	873	2147	5	1.2–2.7	Co	
D10-11C 0-11	1360	3959	12	0–1.2	Co	3474
D10-11D 11-21	1179	2443	13	1.2–2.3	Co	
D10-11E 21-25	1463	3537	13	2.3–2.9	Co	
D11-2B 0-27	891	2347	6	0–4.8	$^{10/9}$Be (ext)	3760
				0–2.7	Co	
D11-2C 27-42	974	**4374**	5	4.8–7.7	$^{10/9}$Be (ext)	
				2.7–4.9	Co	
D11-2D 42-68	**1612**	**3849**	8	**7.7–12.6**	$^{10/9}$Be (ext)	
				4.9–14.5	Co	
D14-16B2 0-14	318	2474	4	0–4.6	$^{10/9}$Be	2155
				0–2.8	Co	
D14-16B3 14-49	651	3841	4	4.6–15.2	$^{10/9}$Be (ext)	
				2.8–13.3	Co	
D14-16B4 49-69	1151	**5199**	4	15.2–21.5	$^{10/9}$Be (ext)	
				13.3–21.9	Co	
D14-16B5 69-97	**1492**	4188	**17**	**21.5–29.6**	$^{10/9}$Be (ext)	
				21.9–27.9	Co	

[a]D2 is off the rise to the east.
[b]Co, cobalt chronometer; ext, extrapolated.
[c]Bold is highest value(s) within a crust if significantly different from other values in that crust.

data were available for the Co chronometer. Growth hiatuses may also contribute to the age disparity between the two methods. As mentioned above, these ages for initiation of crust growth are minima because the Co chronometer and extrapolated Be growth rates do not take into account dissolution and erosion unconformities or periods of non-deposition.

[38] The four thickest crusts analyzed, D7–1 (130 mm), D4–1 (118 mm), D2-3-1 (112 mm), and D14–16B (110 mm) began to grow at 9.4, 13.7, 19.8, and 30.8 Ma ago respectively, based on the

growth rates of individual layers using the Co chronometer and the thickness of each layer. The three thickest crusts progressively increase in water depth (3700, 4000, 4833 m) with increasing age of initiation of growth, and correspondingly a decrease in growth rate. The other thick crust (D14–16B) is from the shallowest water (2155 m), has the slowest growth rate, and is the oldest crust. This crust has growth rates typical of PCZ crusts (75% are ≤5 mm/Myr) based on earlier studies [e.g., *Hein et al.*, 2000].

[39] These results indicate that the dating is internally consistent and as reliable as can be expected based on combined Co and $^{10}Be/^{9}Be$ dating. The uncertainty of the dating for the time period covered by $^{10}Be/^{9}Be$ is a maximum of ±0.5 Myr at 6 Myr. Crust sections deeper than that, where the ages were calculated from Co-chronometry, the uncertainties are greater but the combined $^{10}Be/^{9}Be$ and Co ages clearly demonstrate that these deposits are dateable and reliable archives for past ocean chemistry.

6. Discussion

[40] Several characteristics distinguish Shatsky Rise ferromanganese deposits from those studied from other regions of the global ocean, including deposit configuration, high Cu, Ni, Th, and Li layers in crusts, and a markedly different chemical composition compared to PCZ deposits that occur farther south.

6.1. Amalgamated Crust-Nodule Deposits

[41] The crusts and nodules occur in close proximity on Shatsky Rise, and some nodule deposits were cemented into pavements, thereby forming amalgamated crust-nodule deposits, which were further overgrown by Fe-Mn crust. The nodules formed by accretion about a small nucleus on a sediment surface and the crusts grew on rock surfaces, but in close proximity to the nodules. The amalgamated deposits could have formed either by winnowing of the sediment on which the nodules rested and subsequent crust formation on a rock surface populated with scattered nodules; or the nodule field was so densely packed that crusts were able to grow on that more-or-less continuous hard substrate. Conclusive evidence is not found to support one hypothesis over the other. Since the nodules in the amalgamated deposits are enriched in Cu, Ni, and Li, the sediment was thick enough to have established the diagenetic gradient required to release these metals from their host phases where they then became available to be acquired through adsorption by the nodules at the seabed.

6.2. Spatial and Temporal Enrichments of Cu and Ni in Fe-Mn Crust Layers

[42] Shatsky Rise crusts have much higher average Cu concentrations (Figure 4) and stronger Ni- and Cu-enriched layers than crusts found elsewhere in the global ocean, which may be the result of a deep-water source for those metals not available to shallower-water crusts, or to changes in paleoenvironmental conditions. The strong Cu and Ni enrichments are confined to the deeper layers of the crusts rather than the surface layers, supporting the latter supposition. The Be isotope and Co chronometer ages indicate that this Cu-Ni enrichment is not found in crust layers younger than about 3.4 Ma at any location across Shatsky Rise (Table 9). The exact age of the end of Cu-Ni enrichment at each site is not known because chemical analyses were determined for macroscopically distinct layers within each crust, which might not accurately constrain the compositional changes. However, with the data available, the age of initiation of Cu-Ni-enrichment for the deep-water sites was the middle Miocene (Table 9). Five layers, the most analyzed from a single crust (D4–1), include a layer that accreted prior to enrichment of Cu and Ni, which shows the start of enrichment at about 11 Ma and the end of enrichment at about 3.4 Ma. However, it cannot be ruled out that enrichment started as early as 15–20 Ma at other sites. The three Shatsky Rise deep-water crusts (D3, D4, D7) have the highest Cu concentrations, which correspond to the time interval of about 12.5 to 3.4 Ma. The degree of enrichment decreases in crusts located farther south and the D11–2 site occurs at about the same water depth as D7, but maximum Cu and Ni values are half of what they are in the D7 crust. The deepest-water crust (D2; 4833 m) is at about the same latitude as D7, but is far below the calcite compensation depth (CCD) today and also during the middle Miocene, which likely had an influence on the smaller enrichment of Cu in that crust (Table 9; see below); this is also true for crusts from dredge D8, 4806 m water depth, but not for a nodule analyzed from that dredge. For the shallower-water crust (D14–16B, 2155 m), Cu contents are relatively low throughout the crust, but nonetheless decrease nearly fivefold in the four layers analyzed. This uniform decrease in Cu may reflect a decrease in the extent and intensity of the OMZ during growth of this shallow-water crust.

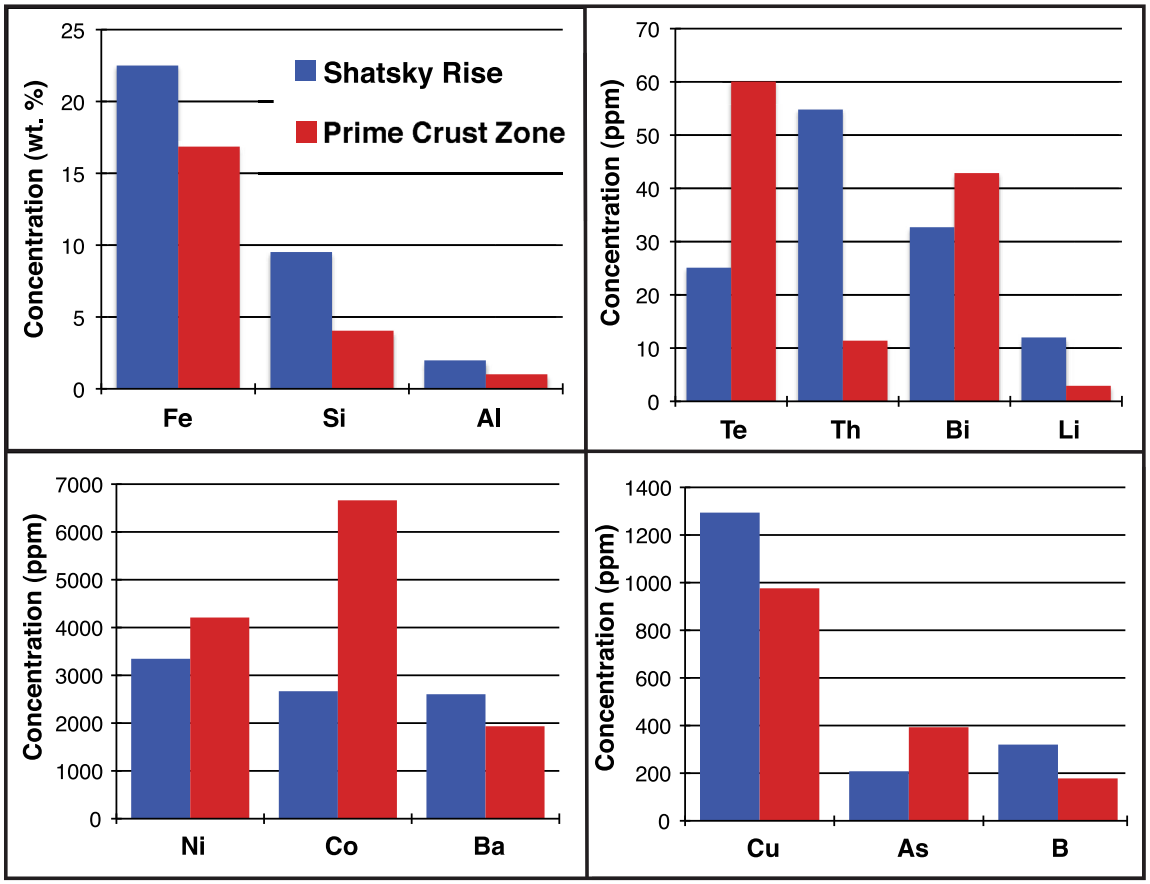

Figure 8. Comparison of Shatsky Rise mean bulk Fe-Mn crust composition for selected elements with mean crust values for northwest-equatorial Pacific Prime Crust Zone, the area of greatest economic interest in the global ocean.

[43] Copper concentrations are highly variable in crusts throughout the area, which reflects water depth and the associated characteristics that change with water depth. For the deep-water crusts, the dominant controls are the composition and flow rate of bottom water masses and the depth of the CCD, which controls sedimentation rate and relative proportions of carbonate, silicate, and organic matter concentrations in bottom sediment, and indirectly pore fluid composition; and for the shallow-water crusts, upwelling along the Rise and extent and intensity of the OMZ. These are discussed in the next section.

6.3. Sources and Enrichment Mechanisms of Cu, Ni, Li, and Th

[44] The chemical composition of crusts and nodules vary on regional, local, and intrasample scales. In general, the chemical composition of nodules is controlled by the ratio of the hydrogenetic to diagenetic components and whether the diagenetic component results from oxic or suboxic diagenesis [*Dymond et al.*, 1984]. The most striking contrasts between the Shatsky Rise crusts and PCZ crusts are the high Fe, Si, Al, B, Ba, Cu, Li, and Th and low Bi, Co, Te, Tl, W, and As concentrations in the Shatsky crusts (Figure 8). The difference in Th concentrations is especially striking in that it is near the Earth's crustal abundance (~12 ppm) for PCZ crusts (11 ppm) yet has a mean of 56 ppm for Shatsky Rise samples and reaches exceptionally high concentrations of 152 ppm for a crust layer from dredge D2 and 113–148 ppm for bulk crusts and a nodule also from D2 (Table 3). The mean Th concentration of the Shatsky Rise crusts is similar to those found in crusts from the Atlantic and Indian Oceans and from seamounts off California in the northeast Pacific (52–56 ppm) [*Hein et al.*, 2000; *Hein and Koschinsky*, 2012]. This enrichment relative to most other Pacific areas may relate to a deep-water source for Th and the location of Shatsky Rise under the Asian dust plume. Dissolved Th concentrations increase systematically

with increasing water depth and are higher than the mean value for Shatsky Rise crusts in three of the four deepest-water sites (D2, D4, D8; but not D3); this depth relation is similar to Indian Ocean crusts (J. R. Hein, USGS unpublished data, 2010). High ^{232}Th is found in the western Pacific under the Asian dust plume [*Nozaki et al.*, 1987], whereas in the central Pacific, ^{232}Th is much lower and without much variability in the water column [*Roy-Barman et al.*, 1996]. The source of ^{232}Th is exclusively detrital material and is a robust tracer of dust fluxes [*Hsieh et al.*, 2011]. In dissolved form, Th is highly particle reactive with a residence time in seawater of <100 years in the North Pacific [*Okubo et al.*, 2012]. Release of Th from bottom water and surface sediment is currently debated and subject of an ongoing GEOTRACES program. Our data indicate that in the deep-water parts of Shatsky Rise, Th is available for scavenging and readily sorbs onto the Fe-Mn oxides. Such availability and bottom scavenging may be temporally and spatially variable in the deep ocean [*Okubo et al.*, 2012].

[45] Another source of Th may be biogenic, which is likely the source for crusts off California where high coastal primary productivity occurs. The deepest-water Shatsky crusts occur below the CCD where organic matter in the sediment is not diluted by pelagic carbonate, so degradation of organic matter and dissolution of biogenic silica may be seabed sources for Th [*Knauss and Ku*, 1983; *Hunter et al.*, 1988; *Moran and Moore*, 1992; *Lao et al.*, 1993]. Biogenic calcite also has high concentrations of Th [*Delaney and Boyle*, 1983], which may provide a source of Th closer to the CCD, currently at about 4200 m [*van Andel et al.*, 1975]. Shatsky Rise occurs below the core of the main midlatitude, pan-Pacific dust plume originating from Asia [e.g., *Rea*, 1994], which is the likely source for variable percentages of other lithogenic elements besides Th, such as Si, Al, K, Be, etc. The dust undergoes dissolution in the water column and can enhance primary productivity.

[46] Cu, Ni, and Li are also strongly enriched in Shatsky Rise samples from the deeper-water sites (Table 3). High concentrations of these three elements in nodules indicate a diagenetic (pore water) source, the greater the diagenetic component the higher the concentration of Li [*Hein and Koschinsky*, 2012]. Hydrogenetic-diagenetic nodules from the Clarion-Clipperton zone (CCZ) in the east Pacific have a mean Li concentration of about 130 ppm, whereas diagenetic nodules from the Peru Basin average about 310 ppm Li; and typical Pacific hydrogenetic crust means are very low, ranging from about 3–7 ppm. Lithium in manganese deposits can also have a hydrothermal source [e.g., *Rogers et al.*, 2001; *Chan and Hein*, 2007], however, the combination of high Cu, Ni, and Li together in the Shatsky Rise crusts indicate a diagenetic source. Such high Li concentrations have not been found in hydrogenetic Fe-Mn crusts and this first occurrence requires explanation. High Li, Cu, and Ni in the nodule layers of amalgamated crust-nodule deposits are the result of diagenetic input to the nodules before they were incorporated into the crusts, which is typical for nodules [e.g., *Halbach et al.*, 1981; *Hein and Koschinsky*, 2012]. However, other crust layers rich in those metals must have another explanation since crusts grow on rock substrates and cannot have a direct diagenetic input [*Hein and Morgan*, 1999]. The most likely explanation is that diagenetic reactions in the sediment (biogenic silica, organic matter) and dissolution of biogenic calcite in the water column are the sources for these elements [e.g., *Martin and Knauer*, 1973; *Boström et al.*, 1974; *Monteiro and Orren*, 1985; *Miller and Cronan*, 1994], which were mixed and enhanced in the deep water masses from which the crusts acquired metals. Similar processes explain Cu and Ni concentrations in the deep-water masses of the NE Atlantic [*Saager et al.*, 1997]. These enrichments would explain the concentrations in the Shatsky Rise crusts that formed in deep water and in places where deep-water upwelled to shallower depths, 2000–3000 m [*Kawabe et al.*, 2009]. The highest concentrations of Li are in crust layers that formed near the CCD while the enriched layers were accreting, from about 12.5 to 3.4 Ma (dredges D3, D4, D7); the CCD varied from about 3900 m to 4300 m during that time [*van Andel et al.*, 1975]. All the Shatsky Rise nodules analyzed have Li concentrations (15–70 ppm) much greater than those found in most Pacific crusts (means of 3–7 ppm), but lower than those found in East Pacific nodules.

[47] Nodules produced from oxic diagenesis have the highest Ni and Cu contents [*Halbach et al.*, 1981], as well as the highest Li contents [*Hein and Koschinsky*, 2012]. Under suboxic diagenetic conditions, accompanied by high contents of organic carbon, abundant Fe^{2+} ions are generated by reduction of ferric iron in sediment pore waters, which outcompetes Cu^{2+}, Ni^{2+}, and Li^{+} for available vacancy sites within the structure of the 10 Å manganate that characterizes nodules, thereby decreasing the contents of metals of economic interest. The

turn-around-point at which Cu and Ni increase with oxic diagenetic input and then decrease with suboxic diagenetic input occurs at an Mn/Fe ratio of about 5 [*Halbach et al.*, 1981]. The high contents of organic carbon in areas of suboxic diagenesis reflect greater primary productivity in surface waters compared to areas where nodule growth is influenced only by oxic diagenetic conditions. Thus, high-grade nodules occur in areas of moderate primary productivity [e.g., *Cronan*, 1980; *Halbach et al.*, 1981; *International Seabed Authority*, 2010]. In addition, the location of nodule/crust accretion relative to the CCD, which is controlled by primary productivity, is important because above that depth biogenic calcite increases sedimentation rates and dilutes organic matter contents [*Verlaan et al.*, 2004; *Cronan*, 2006]. The highest-grade nodules form near, but generally below the CCD.

[48] The Shatsky Rise nodules do not fully comply with this scenario because the redox potential was never low enough to form 10 Å manganate, which is a mineral with tunnel structure that accommodates the high Cu, Ni, and Li concentrations found in nodules in other regions. The δ-MnO_2 mineralogy of Shatsky nodules does not have that tunnel structure. Nonetheless, the data presented here show that δ-MnO_2 can accommodate significant concentrations of Cu, Ni, and Li, all of which correlate with Mn concentrations. The highest Mn/Fe ratio for Shatsky nodules is 2.0, indicating that the nodules did not reach that turn-around-ratio of 5 where the Cu plus Ni concentrations are the highest [*Halbach et al.*, 1981]. These data indicate that the diagenetic production of Cu, Ni, and Li incorporated into the nodules occurred in an oxic environment that was never reducing enough to produce 10 Å manganate, which is also true for the redox potential under which most seamount Fe-Mn crusts formed during the Cenozoic [*Hein et al.*, 2000]. Today, the bottom-water dissolved O_2 content up the flank of Shatsky Rise decreases progressively from about 3.8 ml/l at 4800 m to 2.0 ml/l at 2200 m and is about 3.6 ml/l near the CCD at 4200 m [*Kawabe et al.*, 2009]. Even at the lowest values, which are significantly above 0.1 ml/l characteristic for the suboxic zone, both the nodules and crusts are composed of δ-MnO_2. The abyssal bottom water O_2 content in the CCZ in the eastern Pacific is about the same, 3.8 ml/l [*Mantyla and Reid*, 1983], but the nodules there are composed predominantly of 10 Å manganate and lesser amounts of δ-MnO_2. The difference is that the pore water chemistry is dominated by a lower redox potential in the CCZ and diagenetic reactions produce more Cu, Ni, and Li, but the redox potential is not so low that Fe^{2+} out competes the Cu, Ni, and Li ions for sorption sites. This is validated by the maximum Mn/Fe ratio in Shatsky Rise samples of 2.0, whereas that ratio is up to about 7 for CCZ nodules [*Halbach et al.*, 1981]. An Mn/Fe ratio of about 2.5 divides purely hydrogenetic nodules from those that experienced the beginning of early diagenetic input [*Halbach et al.*, 1981]. Our data indicate that ratio is closer to 2.0 for Shatsky Rise Fe-Mn oxides.

[49] The "fossil" nodules in the Shatsky Rise amalgamated deposits and those currently forming in the area have similar compositions, including high Cu, Ni, and to a lesser degree Li concentrations, with the exception of a nodule from the site of D2, which has a predominantly hydrogenetic signature (high Co). This relationship is not true for the deeper-water, younger crust layers, which are not enriched in those elements. This may be explained by a change in the composition or flow of deep-water masses, which prior to about 3.4 Ma carried the diagenetically produced Cu, Ni, and Li that enriched older crust layers. This present condition is typical of the shallower-water crusts at Shatsky Rise and for crusts elsewhere in the Pacific for both younger and older layers.

[50] The key paleoenvironmental change that may have initiated the chemical changes seen in the deep-water Shatsky Rise crusts during the middle Miocene was the considerable increase in Antarctic glaciation, which most likely enhanced activity of the deep-water masses (increasingly corrosive deep water for carbonates) that accompanied major global cooling. The equator-to-pole thermal gradient increased, which led to an increase in oceanic mixing, and an increased supply of nutrients and primary productivity [e.g., *Kennett and Brunner*, 1973]. Increased continental weathering and eolian input from Asia also increased nutrient supply [e.g., *Leinen and Heath*, 1981]. There was a shift in silica deposition at about 15–12 Ma from the Atlantic to the Pacific [*Cortese et al.*, 2004], accompanied by the beginning of the closure of the Isthmus of Panama to deep-water exchange at about 12 Ma [e.g., *Keigwin*, 1982]. Chemical changes in central Pacific Fe-Mn crusts, including Cu and Ni, occurred at about that time [*Hein et al.*, 1992; *Frank et al.*, 1999]. The Shatsky Rise enrichments of Cu and Ni in crusts ended about 3.4 Ma, which broadly corresponds to initiation of northern hemisphere glaciation, final closing of the Isthmus of Panama,

decreasing activity of AABW, and an increase in eolian dust flux [*Keigwin*, 1982; *Rea*, 1994; *Burton et al.*, 1999].

7. Summary and Conclusions

[51] A unique set of Fe-Mn crust and nodule samples collected from Shatsky Rise, located at middle latitudes in the NW Pacific, show characteristics unlike samples from the PCZ region. One distinction is that the deep-water Shatsky Rise crusts show a diagenetic chemical signal, but not a diagenetic mineralogical signal; that constrains the diagenetic redox conditions to early oxic diagenesis. Diagenetic input of metals to Fe-Mn crusts is rare, although it is unequivocal in these deep-water crusts. Thorium concentrations in PCZ crusts average about 12 ppm, whereas the deep-water Shatsky crusts average 56 ppm, with an exceptionally high concentration of 152 ppm. Thorium enrichments in the older crust layers (pre ~3.4 Ma) reflect movement of Shatsky Rise into the core of the Asian dust plume and additionally deep-water diagenetic sources that enhanced the Cu, Ni, and Li concentrations in the same older crust layers. Crusts and nodules occur in close proximity and some nodule deposits were cemented by and overgrown by crusts forming amalgamated deposits. The non-amalgamated Shatsky Rise deep-water crusts show a diagenetic signal characterized by especially high Cu, Ni, and Li concentrations, which has not been seen in crusts studied elsewhere from the global ocean. This diagenetic input is confined to crust layers older than about 3.4 Ma and began during the middle Miocene. The sources of these metals is most likely from diagenetic reactions that took place in the deep-water sediment (biogenic silica, organic matter) and dissolution of biogenic calcite in the water column, which were mixed and enhanced in the deep water masses from which the crusts acquired metals. The highest concentrations of Li are in crust layers that formed near the CCD. The onset of Ni, Cu, and Li enrichment during the middle Miocene and cessation at about 3.4 Ma were accompanied by changes in the deep-water environment, especially composition and flow rates of water masses; and location of the CCD, which responded to surface water productivity.

[52] The shallower-water crusts (<2500 m) in the PCZ offer a resource potential for Co, Ni, Mn, and perhaps also REEs, Te, Zr, W, and other rare metals, but the Shatsky Rise crusts are less prospective because of the relatively low Co concentrations, deep-water environment, and middle latitude location, which commonly has high seas. The higher Cu, Th, and Li concentrations in Shatsky Rise crusts than found elsewhere in Pacific crusts are, however, not high enough to offset the decreased value related to the lower Co, Te, W, Bi, etc. concentrations (Figure 8). On the other hand, the total REE concentrations in dredge D2 crusts are very high, varying from 0.3 to 0.5%, and therefore warrant further studies in the Ojin Rise Seamounts.

Acknowledgments

[53] Onboard sample descriptions were by Maria Tejada, Glenn Brown, and Atsushi Horio. Warren Smith at SIO facilitated locating and collecting samples. Jutta Heinze carried out the chemical preparation of the samples for Be isotope measurements and Ulrike Westernströer and Dieter Garbe-Schönberg are thanked for the ^{9}Be measurements. Renee Takesue and two anonymous reviewers provided helpful comments that improved this manuscript.

References

Anders, E., and N. Grevesse (1989), Abundances of the elements: Meteoritic and solar, *Geochim. Cosmochim. Acta*, *53*, 197–214, doi:10.1016/0016-7037(89)90286-X.

Beaman, M., W. W. Sager, G. D. Acton, L. Lanci, and J. Pares (2007), Improved Late Cretaceous and early Cenozoic paleomagnetic apparent polar wander path for the Pacific Plate, *Earth Planet. Sci. Lett.*, *262*, 1–20, doi:10.1016/j.epsl.2007.05.036.

Bidoglio, G., P. N. Gibson, M. O'Gorman, and K. J. Roberts (1993), X-ray absorption spectroscopy investigation of surface redox transformations of thallium and chromium on colloidal mineral oxides, *Geochim. Cosmochim. Acta*, *57*, 2389–2394, doi:10.1016/0016-7037(93)90576-I.

Boström, K., O. Joensuu, and I. Brohm (1974), Plankton: Its chemical composition and its significance as a source of pelagic sediments, *Chem. Geol.*, *14*, 255–271, doi:10.1016/0009-2541(74)90063-1.

Burton, K. W., D.-C. Lee, J. N. Christensen, A. N. Halliday, and J. R. Hein (1999), Actual timing of neodymium isotopic variations recorded by Fe-Mn crusts in the western North Atlantic, *Earth Planet. Sci. Lett.*, *171*, 149–156, doi:10.1016/S0012-821X(99)00138-7.

Chan, L.-H., and J. R. Hein (2007), Lithium contents and isotopic compositions of ferromanganese deposits from the global ocean, *Deep Sea Res., Part II*, *54*, 1147–1162, doi:10.1016/j.dsr2.2007.04.003.

Chmeleff, J., F. von Blanckenburg, K. Kossert, and D. Jakob (2010), Determination of the ^{10}Be half-life by multicollector ICP-MS and liquid scintillation counting, *Nucl. Instrum. Methods Phys. Res., Sect. B*, *268*, 192–199, doi:10.1016/j.nimb.2009.09.012.

Cook, H. E., P. D. Johnson, J. C. Matti, and I. Zemmels (1975), Methods of sample preparation and X-ray diffraction data analysis (X-ray mineralogy laboratory, Deep Sea Drilling Project, Univ. of California Riverside), *Initial Rep. Deep Sea Drill. Proj.*, *28*, 999–1007.

Cortese, G., R. Gersonde, C.-D. Hillenbrand, and G. Kuhn (2004), Opal sedimentation shifts in the World Ocean over

the last 15 Myr, *Earth Planet. Sci. Lett.*, *224*, 509–527, doi:10.1016/j.epsl.2004.05.035.

Cronan, D. S. (1980), *Underwater Minerals*, 362 pp., Academic, London.

Cronan, D. S. (2006), Processes in the formation of central Pacific manganese nodule deposits, *J. Mar. Sci. Environ.*, *C4*, 41–48.

Delaney, M. L., and E. A. Boyle (1983), Uranium and thorium isotope concentrations in foraminiferal calcite, *Earth Planet. Sci. Lett.*, *62*, 258–262, doi:10.1016/0012-821X(83)90088-2.

Dymond, J., M. Lyle, B. Finny, D. Z. Piper, K. Murphy, R. Conard, and N. Pisias (1984), Ferromanganese nodules from MANOP Sites H, S, and R—Control of mineralogical and chemical composition by multiple accretionary processes, *Geochim. Cosmochim. Acta*, *48*, 931–949, doi:10.1016/0016-7037(84)90186-8.

Frank, M., J.-D. Eckhardt, A. Eisenhauer, P. W. Kubik, B. Dittrich-Hannen, M. Segl, and A. Mangini (1994), Beryllium 10, thorium 230, and protactinium 231 in Galapagos Microplate sediments: Implications of hydrothermal activity and paleoproductivity changes during the last 100,000 years, *Paleoceanography*, *9*, 559–578, doi:10.1029/94PA01132.

Frank, M., R. K. O'Nions, J. R. Hein, and V. K. Banakar (1999), 60 Myr records of major elements and Pb-Nd isotopes from hydrogenous ferromanganese crusts: Reconstruction of seawater paleochemistry, *Geochim. Cosmochim. Acta*, *63*, 1689–1708, doi:10.1016/S0016-7037(99)00079-4.

Garbe-Schönberg, C. D. (1993), Simultaneous determination of 37 trace elements in 28 international rock standards by ICP-MS, *Geostand. Newsl.*, *17*, 81–97, doi:10.1111/j.1751-908X.1993.tb00122.x.

Halbach, P., C. Scherhag, U. Hebisch, and V. Marchig (1981), Geochemical and mineralogical control of different genetic types of deep-sea nodules from the Pacific Ocean, *Miner. Deposita*, *16*, 59–84, doi:10.1007/BF00206455.

Hein, J. R., and A. Koschinsky (2012), Deep-ocean ferromanganese crusts and nodules, in *Treatise on Geochemistry*, vol. 12, edited by S. Scott, Elsevier, New York, in press.

Hein, J. R., and C. L. Morgan (1999), Influence of substrate rocks on Fe-Mn crust composition, *Deep Sea Res., Part I*, *46*, 855–875, doi:10.1016/S0967-0637(98)00097-1.

Hein, J. R., W. C. Schwab, and A. S. Davis (1988), Cobalt and platinum-rich ferromanganese crusts and associated substrate rocks from the Marshall Islands, *Mar. Geol.*, *78*, 255–283, doi:10.1016/0025-3227(88)90113-2.

Hein, J. R., W. A. Bohrson, M. S. Schulz, M. Noble, and D. A. Clague (1992), Variations in the fine-scale composition of a central Pacific ferromanganese crust: Paleoceanographic implications, *Paleoceanography*, *7*, 63–77, doi:10.1029/91PA02936.

Hein, J. R., H.-W. Yeh, S. H. Gunn, W. V. Sliter, L. M. Benninger, and C.-H. Wang (1993), Two major Cenozoic episodes of phosphogenesis recorded in equatorial Pacific seamount deposits, *Paleoceanography*, *8*, 293–311, doi:10.1029/93PA00320.

Hein, J. R., A. Koschinsky, M. Bau, F. T. Manheim, J.-K. Kang, and L. Roberts (2000), Cobalt-rich ferromanganese crusts in the Pacific, in *Handbook of Marine Mineral Deposits*, edited by D. S. Cronan, pp. 239–279, CRC Press, Boca Raton, Fla.

Hein, J. R., A. Koschinsky, and B. R. McIntyre (2005), Mercury- and silver-rich ferromanganese-oxides, Southern California Borderland: Deposit model and environmental implications, *Econ. Geol.*, *100*(6), 1151–1168, doi:10.2113/gsecongeo.100.6.1151.

Hein, J. R., T. A. Conrad, and R. E. Dunham (2009), Seamount characteristics and mine-site model applied to exploration- and mining-lease-block selection for cobalt-rich ferromanganese crusts, *Mar. Georesour. Geotechnol.*, *27*, 160–176, doi:10.1080/10641190902852485.

Hsieh, Y.-T., G. M. Henderson, and A. L. Thomas (2011), Combining seawater ^{232}Th and ^{230}Th concentrations to determine dust fluxes to the surface ocean, *Earth Planet. Sci. Lett.*, *312*, 280–290, doi:10.1016/j.epsl.2011.10.022.

Hunter, K. A., D. J. Hawke, and L. K. Choo (1988), Equilibrium adsorption of thorium by metal oxides in marine electrolytes, *Geochim. Cosmochim. Acta*, *52*, 627–636, doi:10.1016/0016-7037(88)90324-9.

International Seabed Authority (2010), A geological model of polymetallic nodule deposits in the Clarion-Clipperton fracture zone, *ISA Tech. Study, 6*, Kingston, Jamaica.

Kawabe, M., S. Fujio, D. Yanagimoto, and K. Tanaka (2009), Water masses and currents of deep-circulation southwest of the Shatsky Rise in the western North Pacific, *Deep Sea Res., Part I*, *56*, 1675–1687, doi:10.1016/j.dsr.2009.06.003.

Keigwin, L. (1982), Isotopic paleoceanography of the Caribbean and East Pacific: Role of Panama uplift in late Neogene time, *Science*, *217*, 350–353, doi:10.1126/science.217.4557.350.

Kennett, J. P., and C. A. Brunner (1973), Antarctic Late Cenozoic glaciation: Evidence for initiation of ice rafting and inferred increased bottom-water activity, *Geol. Soc. Am. Bull.*, *84*, 2043–2052, doi:10.1130/0016-7606(1973)84<2043:ALCGEF>2.0.CO;2.

Klovan, J. E., and J. Imbrie (1971), An algorithm and FORTRAN-IV program for large-scale Q-mode factor analysis and calculation of factor scores, *Math. Geol.*, *3*, 61–77, doi:10.1007/BF02047433.

Knauss, K., and T.-L. Ku (1983), The elemental composition and decay-series radio-nuclide content of plankton from the east Pacific, *Chem. Geol.*, *39*, 125–145, doi:10.1016/0009-2541(83)90076-1.

Korschinek, G., et al. (2010), A new value for the half-life of ^{10}Be by heavy-ion elastic recoil detection and liquid scintillation counting, *Nucl. Instrum. Methods Phys. Res., Sect. B*, *268*, 187–191, doi:10.1016/j.nimb.2009.09.020.

Koschinsky, A., and P. Halbach (1995), Sequential leaching of marine ferromanganese precipitates: Genetic implications, *Geochim. Cosmochim. Acta*, *59*, 5113–5132, doi:10.1016/0016-7037(95)00358-4.

Koschinsky, A., and J. R. Hein (2003), Uptake of elements from seawater by ferromanganese crusts: Solid phase association and seawater speciation, *Mar. Geol.*, *198*, 331–351, doi:10.1016/S0025-3227(03)00122-1.

Kubik, P. W., and M. Christl (2010), ^{10}Be and ^{26}Al measurements at the Zurich 6 MV Tandem AMS facility, *Nucl. Instrum. Methods Phys. Res., Sect. B*, *268*, 880–883, doi:10.1016/j.nimb.2009.10.054.

Lao, Y., R. F. Anderson, W. S. Broecker, H. J. Hofmann, and W. Wolfli (1993), Particulate fluxes of ^{230}Th, ^{231}Pa, and ^{10}Be in the northeastern Pacific Ocean, *Geochim. Cosmochim. Acta*, *57*, 205–217, doi:10.1016/0016-7037(93)90479-G.

Leinen, M., and G. R. Heath (1981), Sedimentary indicators of atmospheric activity in the northern hemisphere during the Cenozoic, *Palaeogeogr. Palaeoclimatol. Palaeoecol.*, *36*, 1–21, doi:10.1016/0031-0182(81)90046-8.

Leinen, M., J. M. Prospero, E. Arnold, and M. Blank (1994), Mineralogy of aeolian dust reaching the North Pacific Ocean: 1. Sampling and analysis, *J. Geophys. Res.*, *99*, 21,017–21,023, doi:10.1029/94JD01735.

Mahoney, J. J., R. A. Duncan, M. L. G. Tejada, W. W. Sager, and T. J. Bralower (2005), Jurassic-Cretaceous boundary age and mid-ocean-ridge-type mantle source for Shatsky Rise, *Geology*, *33*, 185–188, doi:10.1130/G21378.1.

Manheim, F. T., and C. M. Lane-Bostwick (1988), Cobalt in ferromanganese crusts as a monitor of hydrothermal discharge on the sea floor, *Nature*, *335*, 59–62, doi:10.1038/335059a0.

Mantyla, A. W., and J. L. Reid (1983), Abyssal characteristics of the world ocean waters, *Deep Sea Res.*, *30*, 805–833, doi:10.1016/0198-0149(83)90002-X.

Martin, J. H., and G. A. Knauer (1973), The elemental composition of plankton, *Geochim. Cosmochim. Acta*, *37*, 1639–1653, doi:10.1016/0016-7037(73)90154-3.

McLennan, S. M. (1989), Rare earth elements in sedimentary rocks: Influence of provenance and sedimentary processes, in *Geochemistry and Mineralogy of Rare Earth Elements*, *Rev. Mineral.*, vol. 21, edited by B. R. Lipin and G. A. McKay, pp. 169–200, Mineral. Soc. of Am., Washington, D. C.

Miller, S., and D. S. Cronan (1994), Element supply to surface sediments and interrelationships with nodules along the Aitutaki-Jarvis Transect, South Pacific, *J. Geol. Soc.*, *151*, 403–412, doi:10.1144/gsjgs.151.2.0403.

Monteiro, P. M. S., and M. J. Orren (1985), Trace metals in the southern ocean: On the geochemistry of copper, *Mar. Chem.*, *15*, 345–355, doi:10.1016/0304-4203(85)90045-3.

Moran, S. B., and R. M. Moore (1992), Kinetics of the removal of dissolved aluminum by diatoms in seawater: A comparison with thorium, *Geochim. Cosmochim. Acta*, *56*, 3365–3374, doi:10.1016/0016-7037(92)90384-U.

Müller, A. M., M. Christl, J. Lachner, M. Suter, and H.-A. Synal (2010), Competitive ^{10}Be measurements below 1 MeV with the upgraded ETH–TANDY AMS facility, *Nucl. Instrum. Methods Phys. Res., Sect. B*, *268*(17–18), 2801–2807, doi:10.1016/j.nimb.2010.05.104.

Murray, J. W., and J. G. Dillard (1979), The oxidation of cobalt(II) adsorbed on manganese dioxide, *Geochim. Cosmochim. Acta*, *43*, 781–787, doi:10.1016/0016-7037(79)90261-8.

Nakanishi, M., W. W. Sager, and A. Klaus (1999), Magnetic lineations within Shatsky Rise, northwest Pacific Ocean: Implications for hot spot-triple junction interaction and oceanic plateau formation, *J. Geophys. Res.*, *104*, 7539–7556, doi:10.1029/1999JB900002.

Nozaki, Y., H.-S. Yang, and M. Yamada (1987), Scavenging of thorium in the ocean, *J. Geophys. Res.*, *92*, 772–778, doi:10.1029/JC092iC01p00772.

Okubo, A., H. Obata, T. Gamo, and M. Yamada (2012), ^{230}Th and ^{232}Th distributions in mid-latitudes of the North Pacific Ocean: Effect of bottom scavenging, *Earth Planet. Sci. Lett.*, *339–340*, 139–150, doi:10.1016/j.epsl.2012.05.012.

Rea, D. K. (1994), The paleoclimatic record provided by eolian deposition in the deep sea: The geologic history of wind, *Rev. Geophys.*, *32*, 159–195, doi:10.1029/93RG03257.

Rogers, T. D. S., R. A. Hodkinson, and D. S. Cronan (2001), Hydrothermal manganese deposits form the Tonga-Kermadec Ridge and Lau Basin Region, Southwest Pacific, *Mar. Georesour. Geotechnol.*, *19*, 245–268, doi:10.1080/106411901753335326.

Roy-Barman, M., J. H. Chen, and G. J. Wasserburg (1996), ^{230}Th -^{232}Th systematics in the central Pacific Ocean: The sources and the fates of thorium, *Earth Planet. Sci. Lett.*, *139*, 351–363, doi:10.1016/0012-821X(96)00017-9.

Saager, P. M., H. J. W. de Baar, J. T. M. de Jong, R. F. Nolting, and J. Schijf (1997), Hydrography and local sources of dissolved trace metals Mn, Ni, Cu, and Cd in the northeast Atlantic Ocean, *Mar. Chem.*, *57*, 195–216, doi:10.1016/S0304-4203(97)00038-8.

Sager, W. W. (2005), What built Shatsky Rise, a mantle plume or ridge tectonics?, in *Plates, Plumes, and Paradigms*, edited by G. R. Foulger et al., *Spec. Pap. Geol. Soc. Am.*, *388*, 721–733, doi:10.1130/0-8137-2388-4.721.

Sager, W. W. (2006), Cretaceous paleomagnetic apparent polar wander path for the Pacific plate calculated from Deep Sea Drilling Project and Ocean Drilling Program basalt cores, *Phys. Earth Planet. Inter.*, *156*, 329–349, doi:10.1016/j.pepi.2005.09.014.

Sager, W. W., and H.-C. Han (1993), Rapid formation of the Shatsky Rise oceanic plateau inferred from its magnetic anomaly, *Nature*, *364*, 610–613, doi:10.1038/364610a0.

Sager, W. W., J. Kim, A. Klaus, M. Nakanishi, and L. M. Khankishieva (1999), Bathymetry of Shatsky Rise, northwest Pacific Ocean: Implications for ocean plateau development at a triple junction, *J. Geophys. Res.*, *104*, 7557–7576, doi:10.1029/1998JB900009.

Tatsumi, Y., H. Shinjoe, H. Ishizuka, W. W. Sager, and A. Klaus (1998), Geochemical evidence for a mid-Cretaceous superplume, *Geology*, *26*, 151–154, doi:10.1130/0091-7613(1998)026<0151:GEFAMC>2.3.CO;2.

van Andel, T. H., G. R. Heath, and T. C. Moore Jr. (1975), Cenozoic History and Paleoceanography of the Central Equatorial Pacific Ocean, *Mem. Geol. Soc. Am.*, *143*, 134 pp.

Verlaan, P. A., D. S. Cronan, and C. L. Morgan (2004), A comparative analysis of compositional variations in and between marine ferromanganese nodules and crusts in the South Pacific and their environmental controls, *Prog. Oceanogr.*, *63*, 125–158, doi:10.1016/j.pocean.2004.11.001.